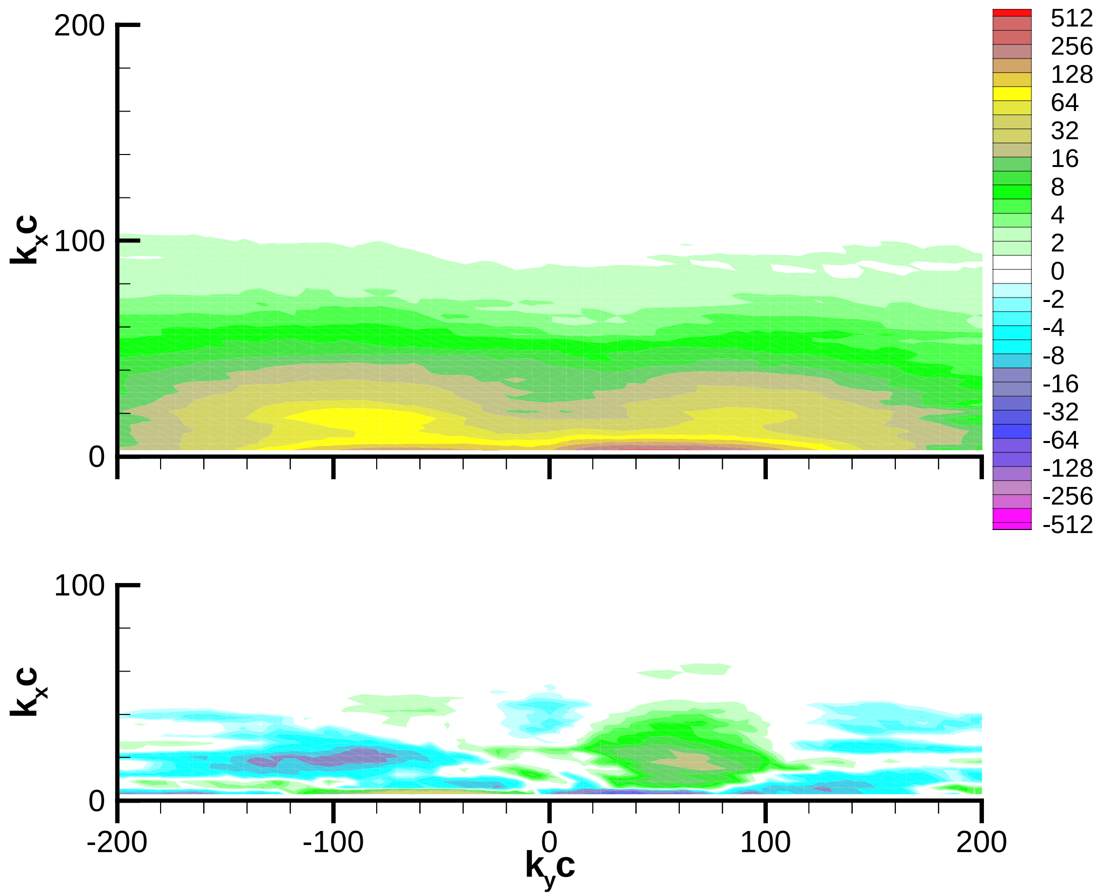


Figure 4.24

Wave number frequency spectrum of the axial ($u$) velocity component calculated for two-point profile C4 (see figure 4.9). Contours of the real component of $\frac{\phi_{uu}}{\overline{u^2}c^2}\times 10^6$ are shown on top and the imaginary part on bottom.

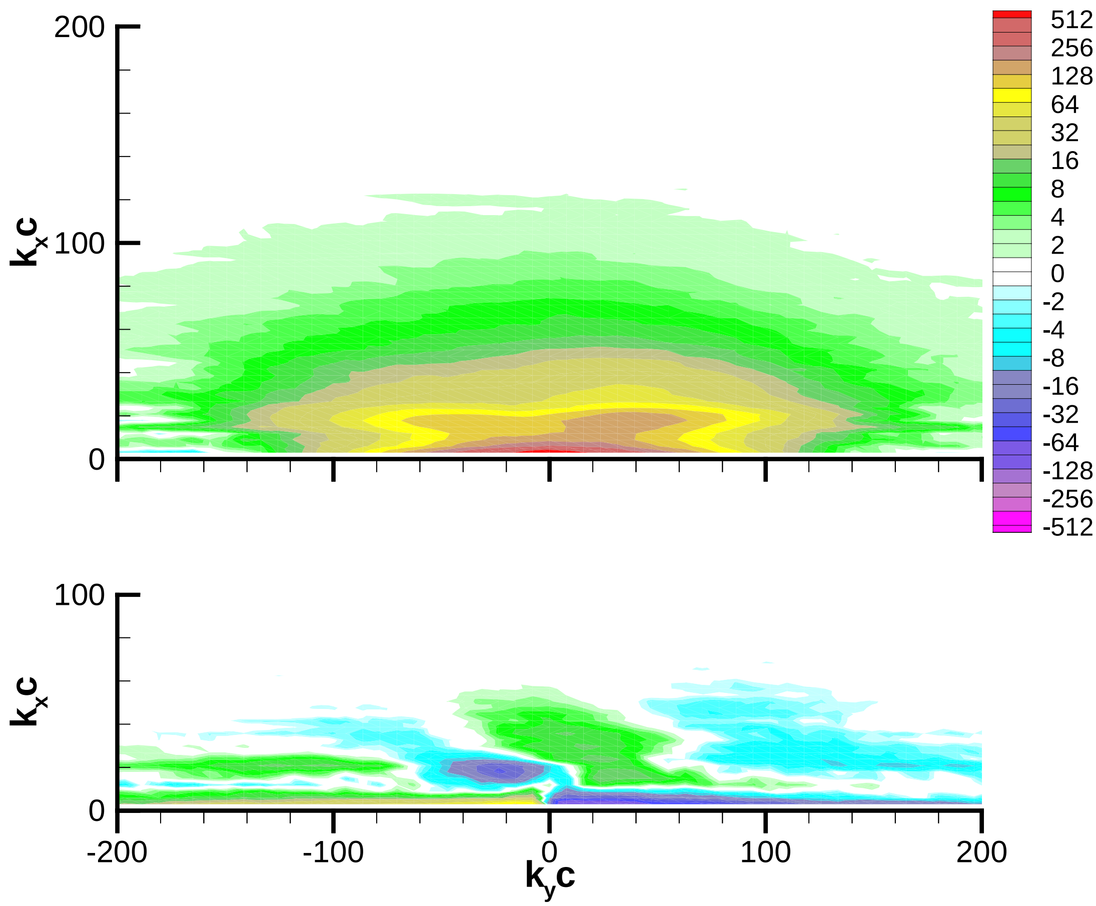


Figure 4.25

Wave number frequency spectrum of the spanwise ($v$) velocity component calculated for two-point profile C4 (see figure 4.9). Contours of the real component of $\frac{\phi_{vv}}{\overline{v^2}c^2}\times 10^6$ are shown on top and the imaginary part on bottom.

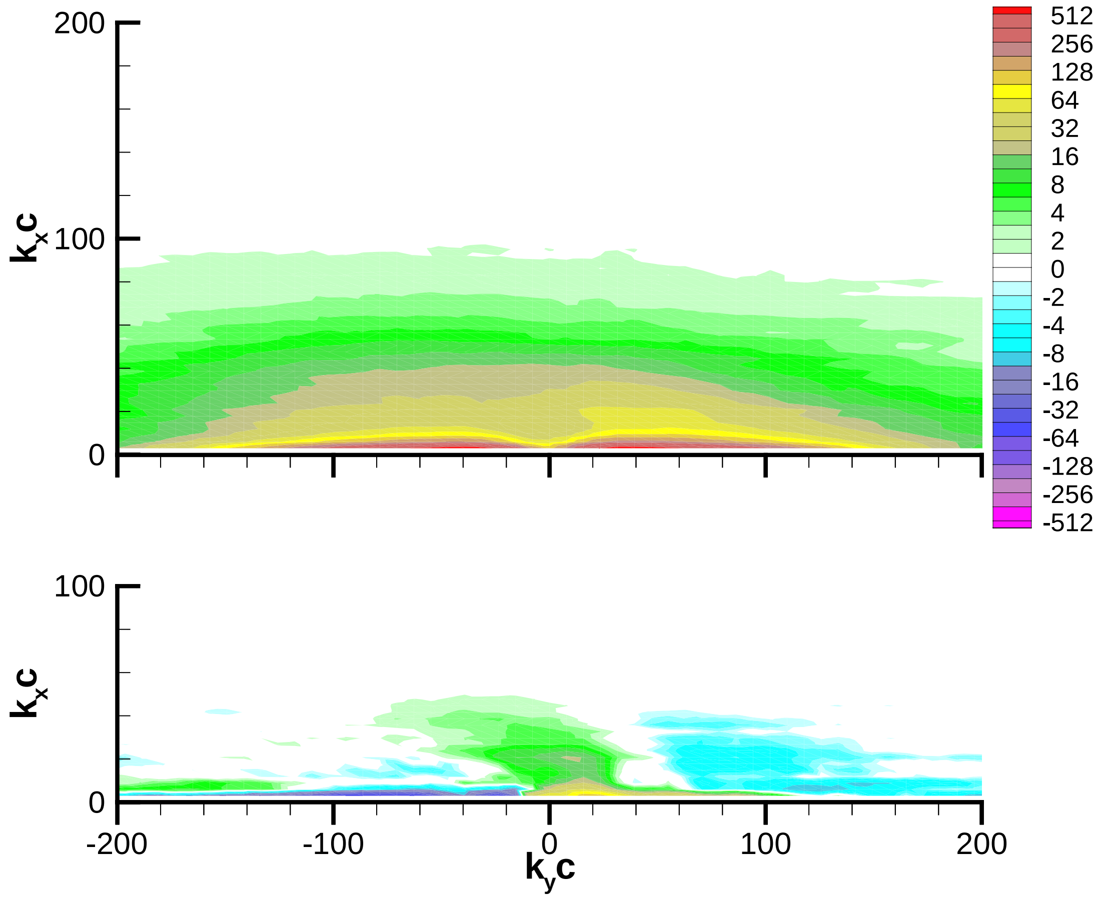


Figure 4.26

Wave number frequency spectrum of the upwash ($w$) velocity component calculated for two-point profile C4 (see figure 4.9). Contours of the real component of $\frac{\phi_{ww}}{\overline{w^2}c^2}\times 10^6$ are shown on top and the imaginary part on bottom.

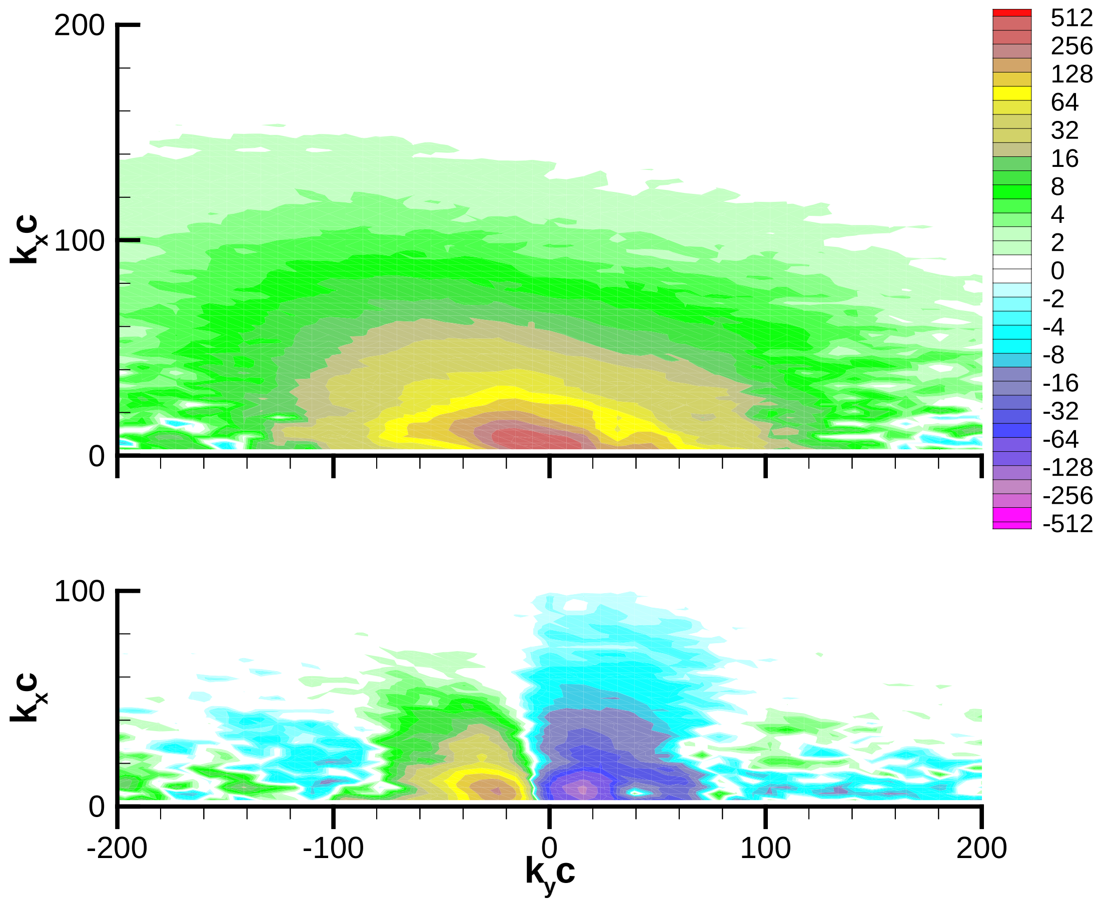


Figure 4.27

Wave number frequency spectrum of the axial ($u$) velocity component calculated for two-point profile C5 (see figure 4.9). Contours of the real component of $\frac{\phi_{uu}}{\overline{u^2}c^2}\times 10^6$ are shown on top and the imaginary part on bottom.

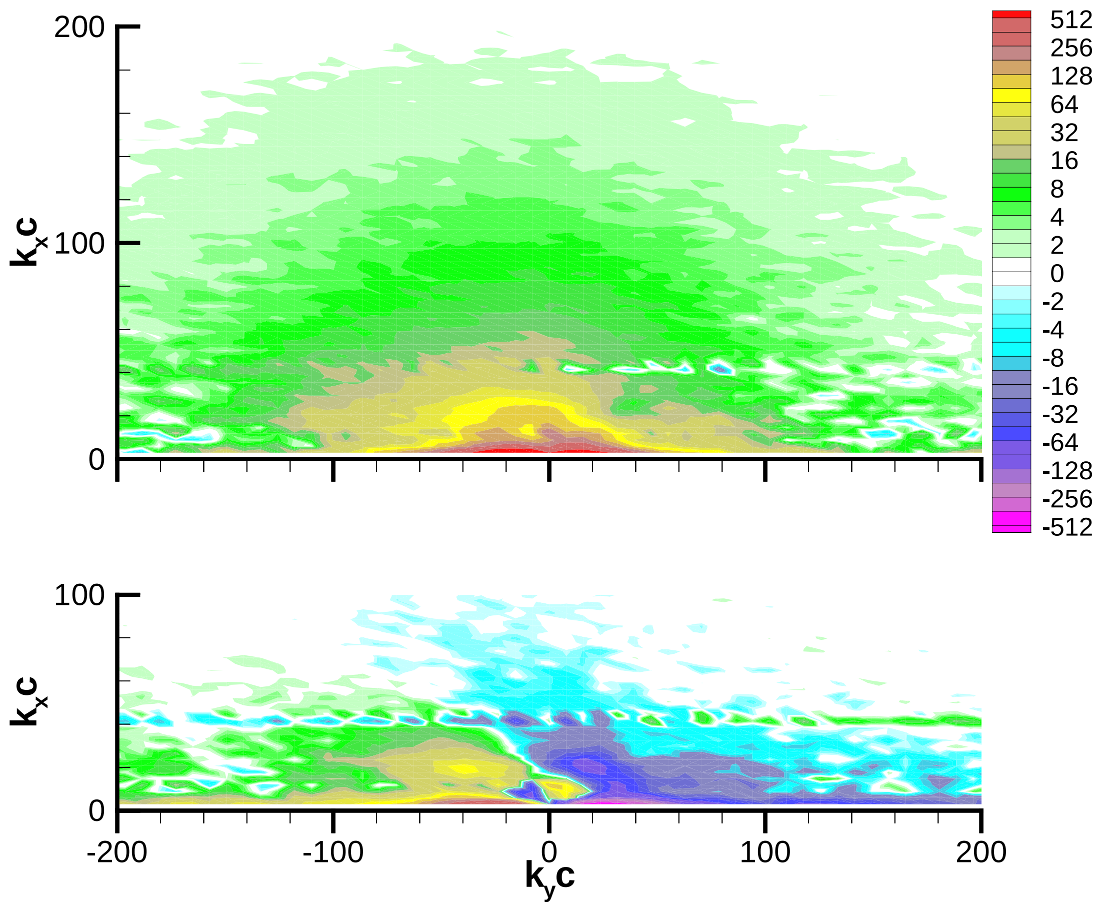


Figure 4.28

Wave number frequency spectrum of the spanwise ($v$) velocity component calculated for two-point profile C5 (see figure 4.9). Contours of the real component of $\frac{\phi_{vv}}{\overline{v^2}c^2}\times 10^6$ are shown on top and the imaginary part on bottom.

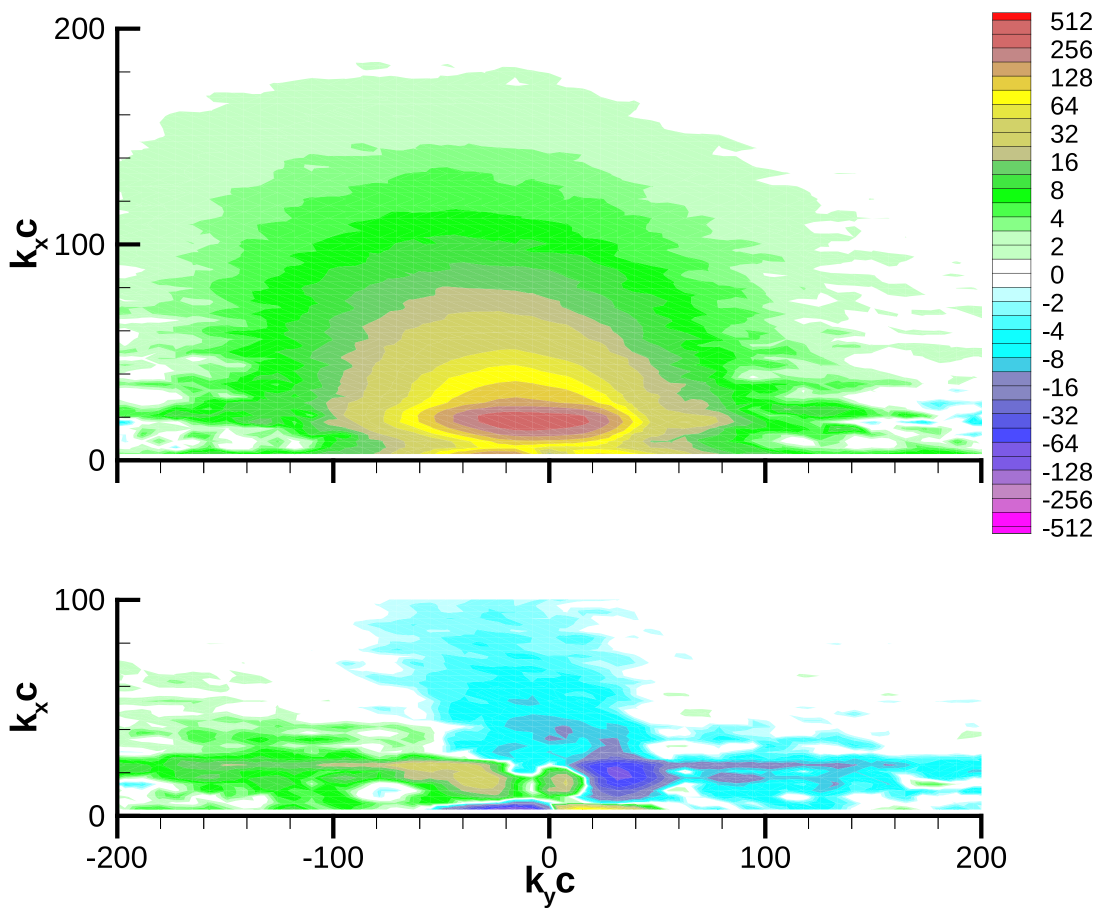


Figure 4.29

Wave number frequency spectrum of the upwash ($w$) velocity component calculated for two-point profile C5 (see figure 4.9). Contours of the real component of $\dfrac{\phi_{ww}}{\overline{w^2}c^2}\times 10^6$ are shown on top and the imaginary part on bottom.

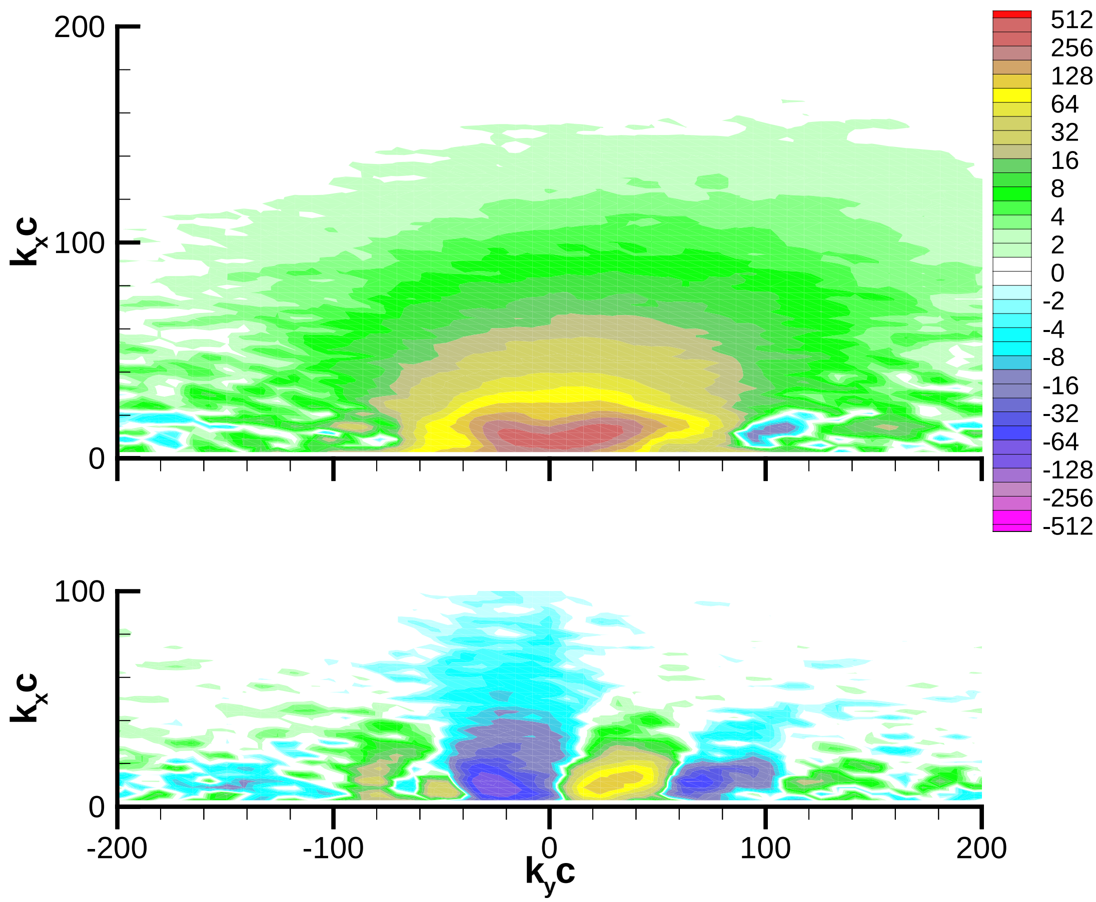


Figure 4.30

Wave number frequency spectrum of the axial ($u$) velocity component calculated for two-point profile C1 (see figure 4.9). Contours of the real component of $\frac{\phi_{uu}}{\overline{u^2}c^2}\times 10^6$ are shown on top and the imaginary part on bottom.

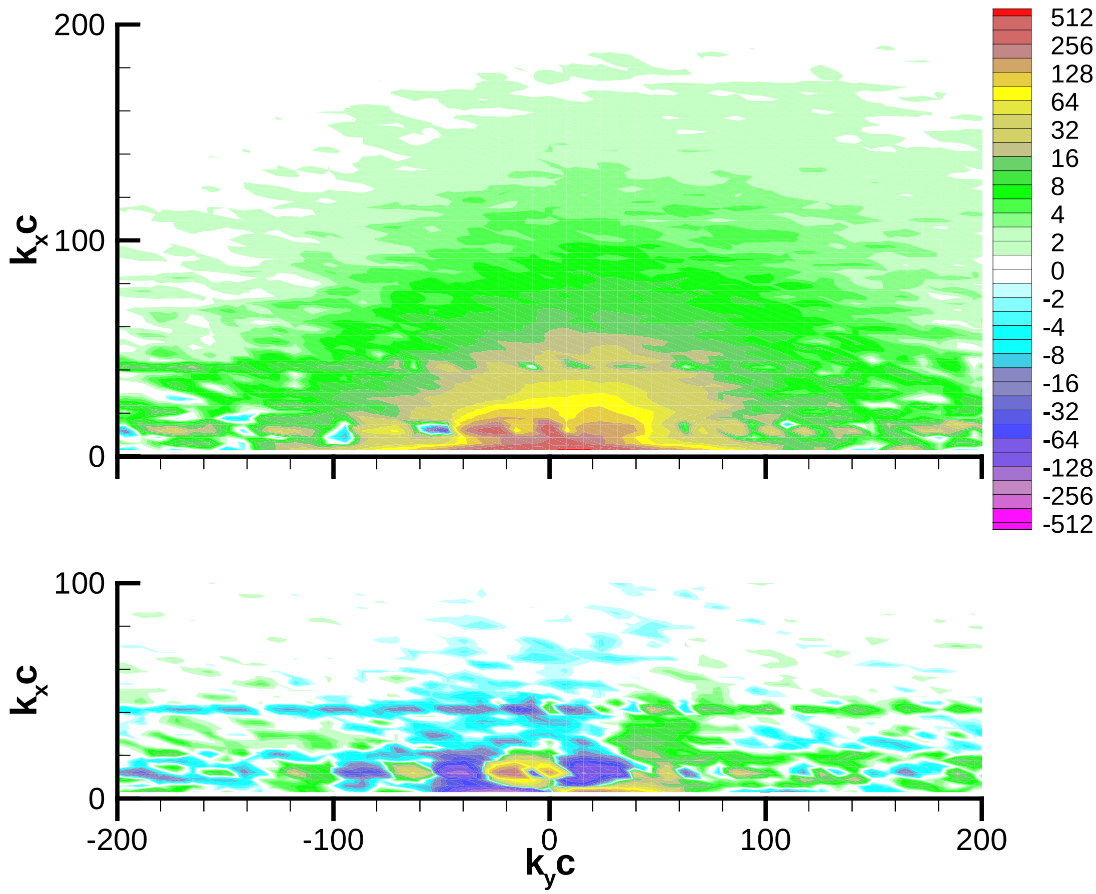


Figure 4.31

Wave number frequency spectrum of the spanwise ($v$) velocity component calculated for two-point profile C1 (see figure 4.9). Contours of the real component of $\frac{\phi_{vv}}{\overline{v^2}c^2}\times 10^6$ are shown on top and the imaginary part on bottom.

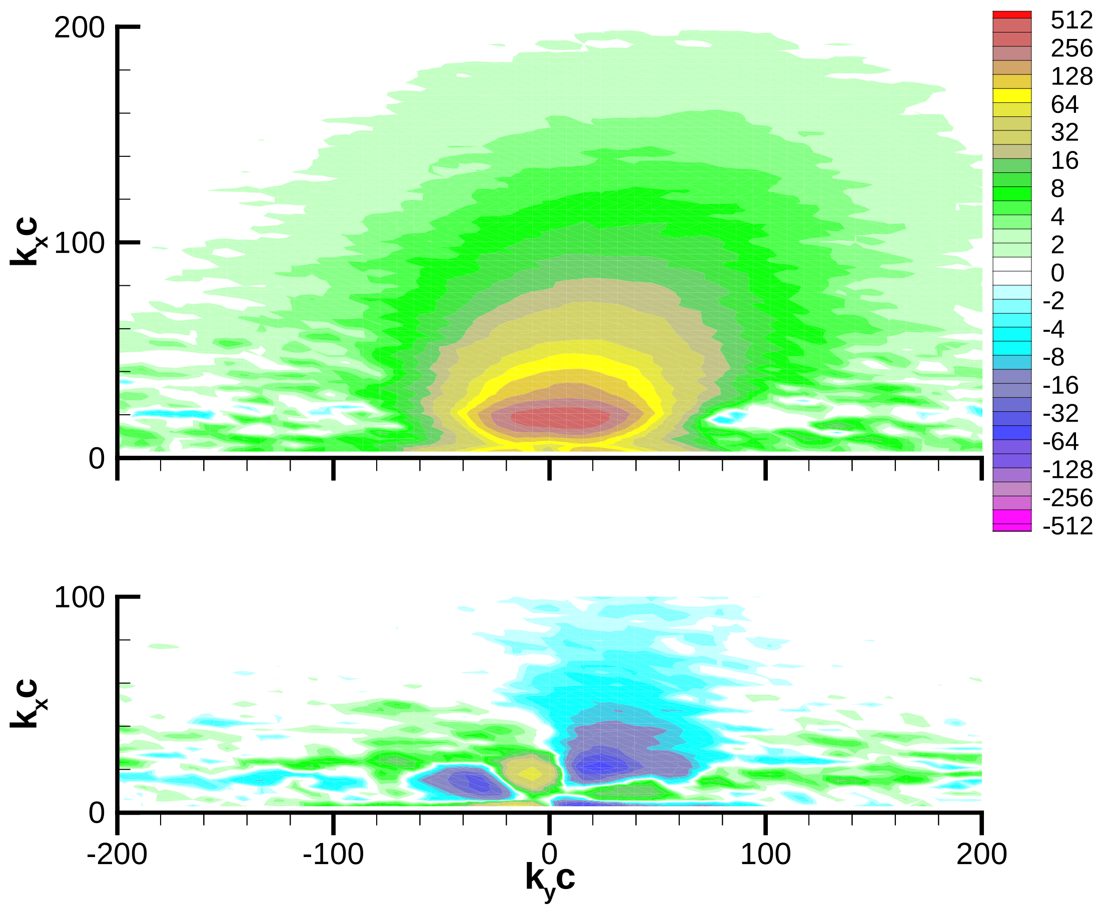


Figure 4.32

Wave number frequency spectrum of the upwash ($w$) velocity component calculated for two-point profile C1 (see figure 4.9). Contours of the real component of $\frac{\phi_{ww}}{\overline{w^2}c^2}\times 10^6$ are shown on top and the imaginary part on bottom.

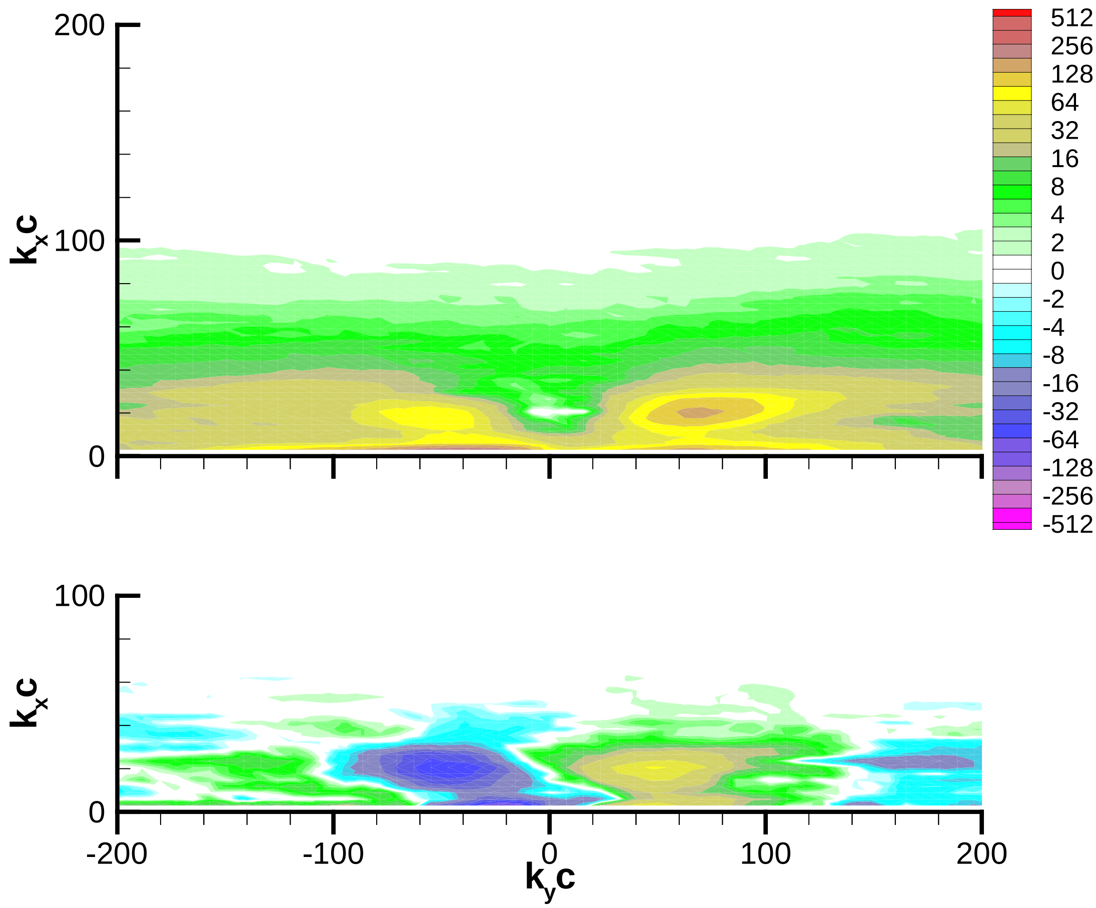


Figure 4.33

Wave number frequency spectrum of the axial ($u$) velocity component calculated for two-point profile C2 (see figure 4.9). Contours of the real component of $\frac{\phi_{uu}}{\overline{u^2}c^2}\times 10^6$ are shown on top and the imaginary part on bottom.

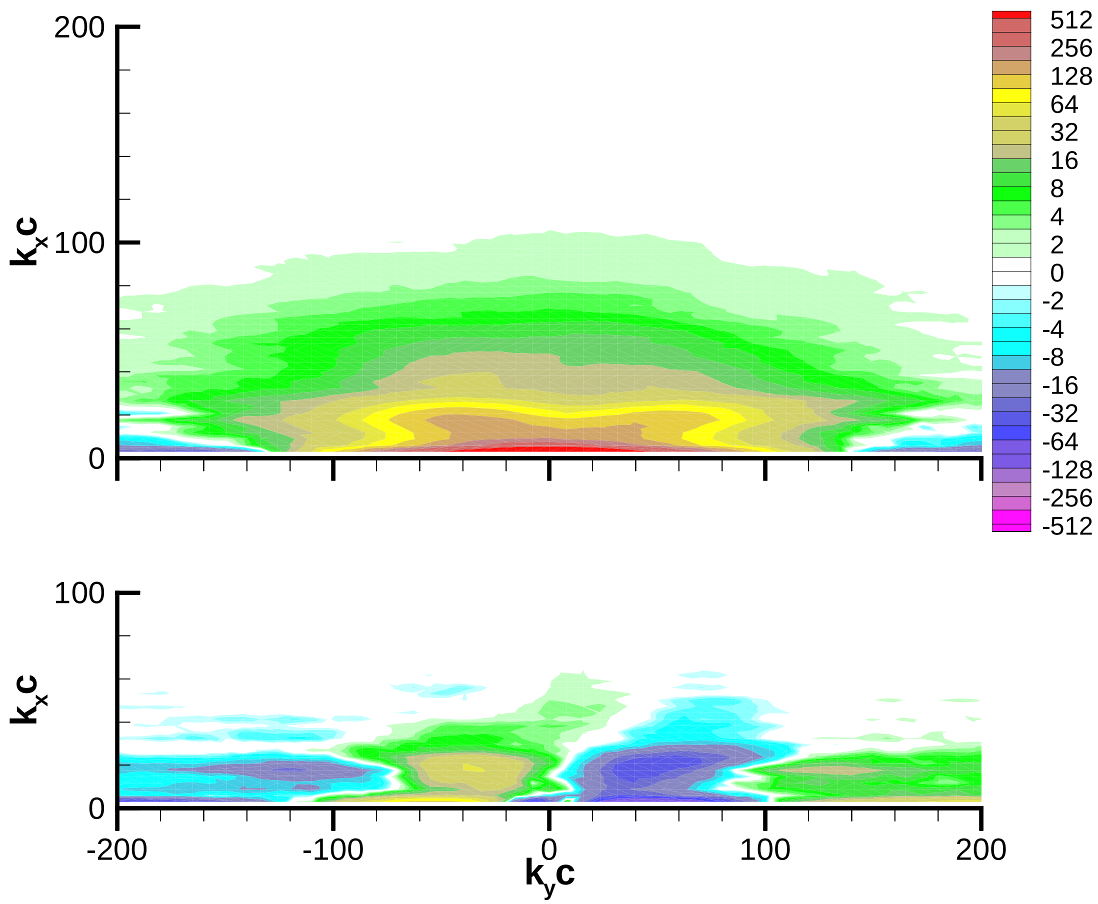


Figure 4.34

Wave number frequency spectrum of the spanwise ($v$) velocity component calculated for two-point profile C2 (see figure 4.9). Contours of the real component of $\frac{\phi_{vv}}{\overline{v^2}c^2}\times 10^6$ are shown on top and the imaginary part on bottom.

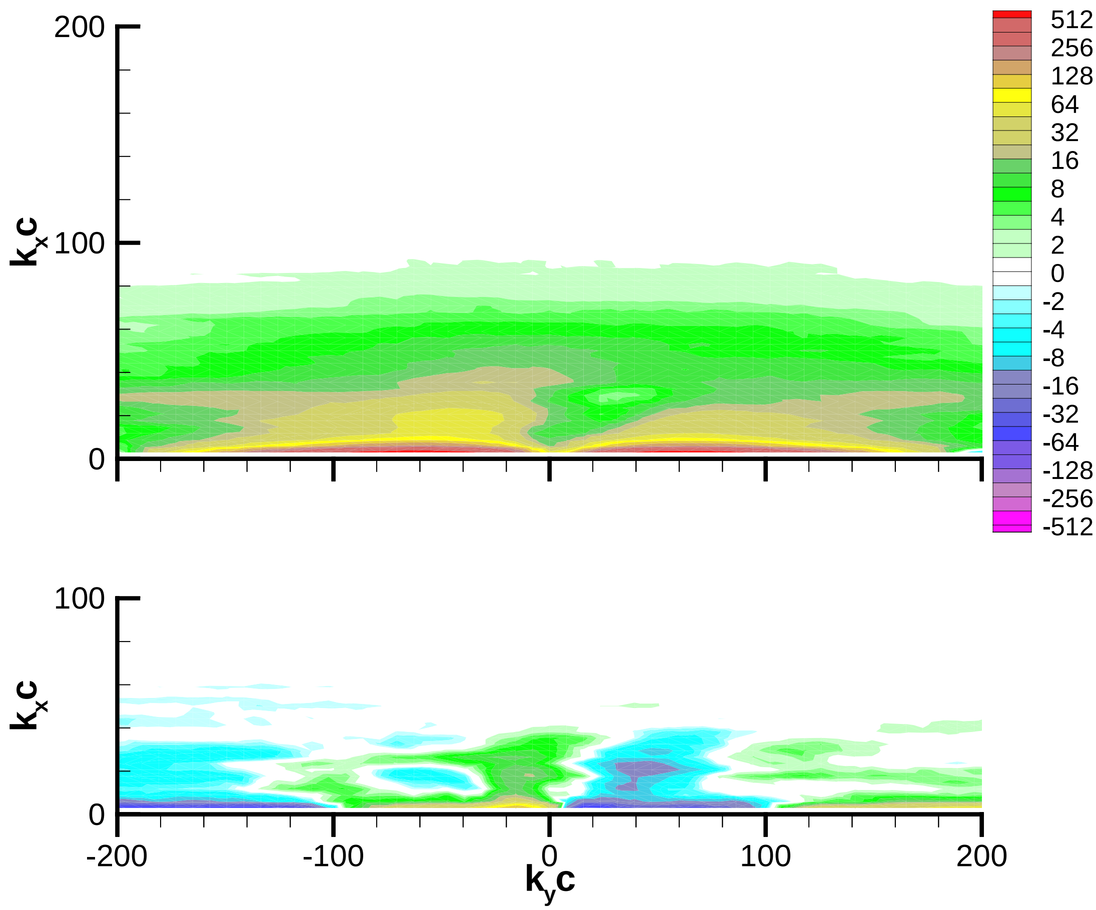


Figure 4.35

Wave number frequency spectrum of the upwash ($w$) velocity component calculated for two-point profile C2 (see figure 4.9). Contours of the real component of $\frac{\phi_{ww}}{\overline{w^2} c^2} \times 10^6$ are shown on top and the imaginary part on bottom.

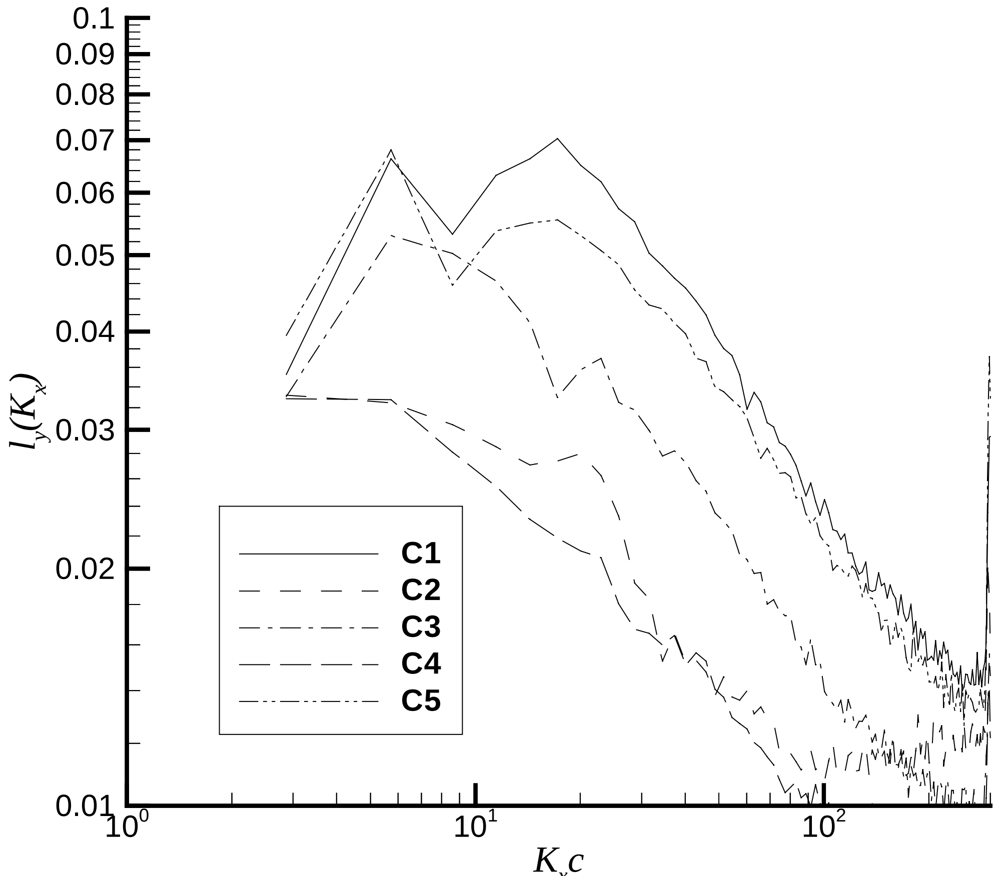


Figure 4.36

Upwash correlation length scales (defined in equation 3.8) for profiles C1 - C5.

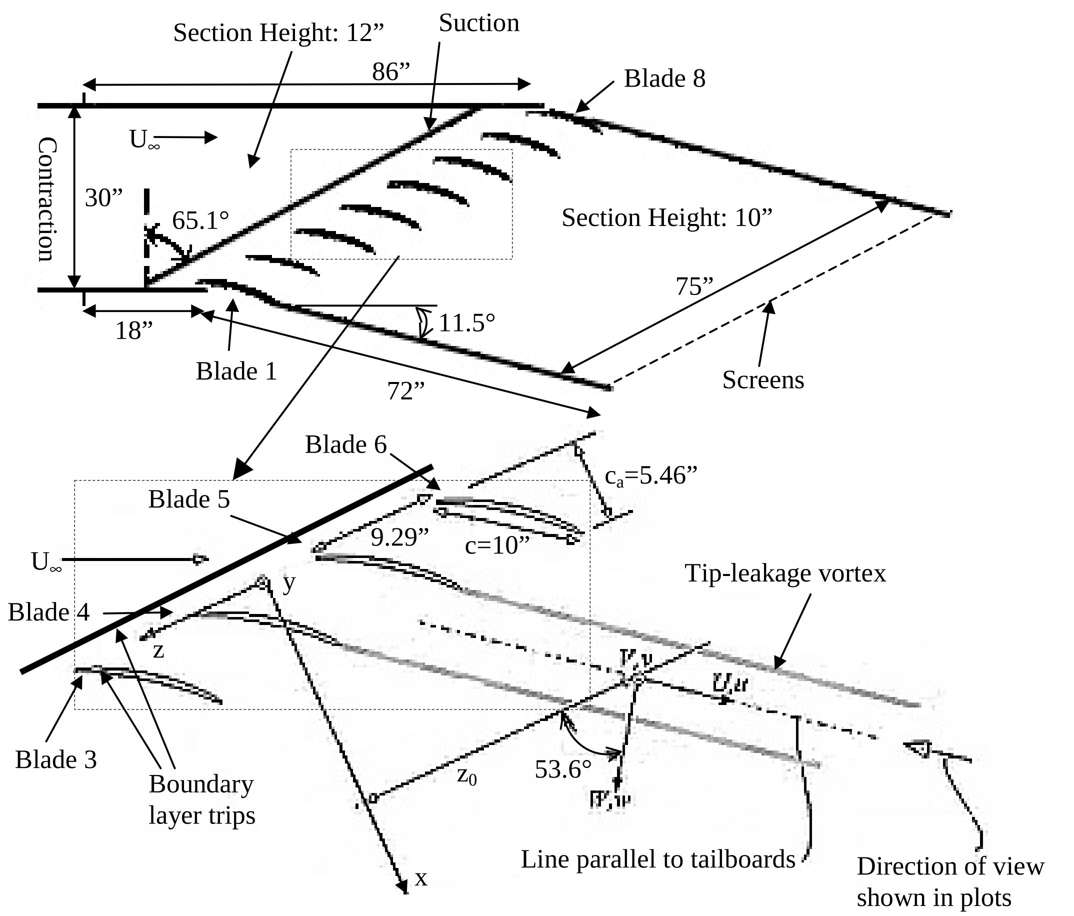


Figure 5.1

A schematic showing the design of the Virginia Tech Low Speed Cascade Wind Tunnel.

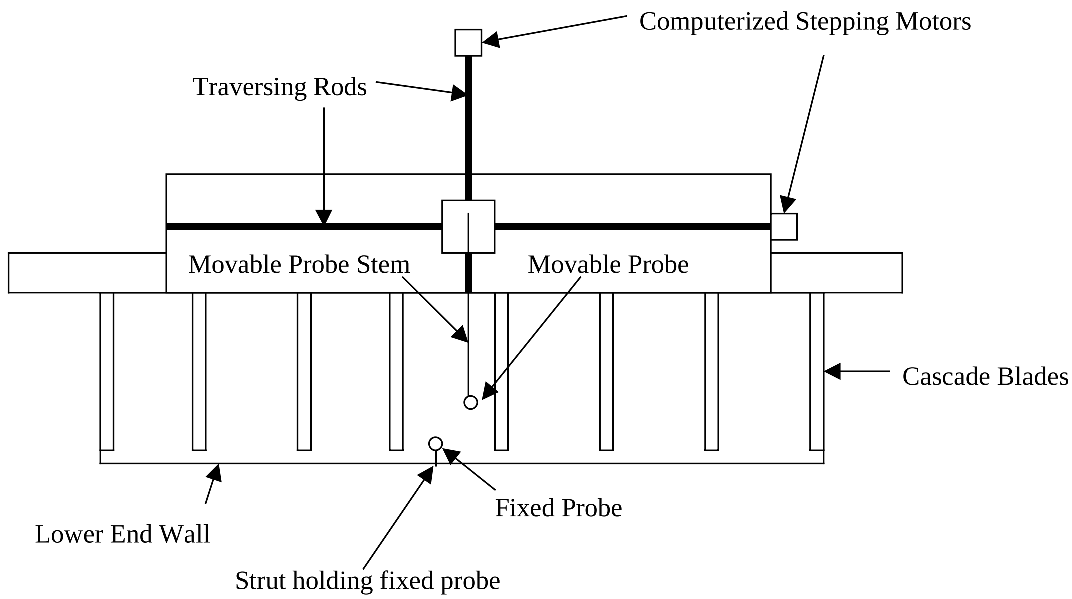


Figure 5.2

A diagram showing the probe mounting arrangement used to take the two-point measurements. This is a cross-sectional view of the test section. The fixed probe is held by a strut attached to the lower end wall, while the movable probe is held by a stem extending into the test section through a slot in the upper end wall. The movable probe stem is attached to a two axis computerized traverse that sits on the top of the wind tunnel.

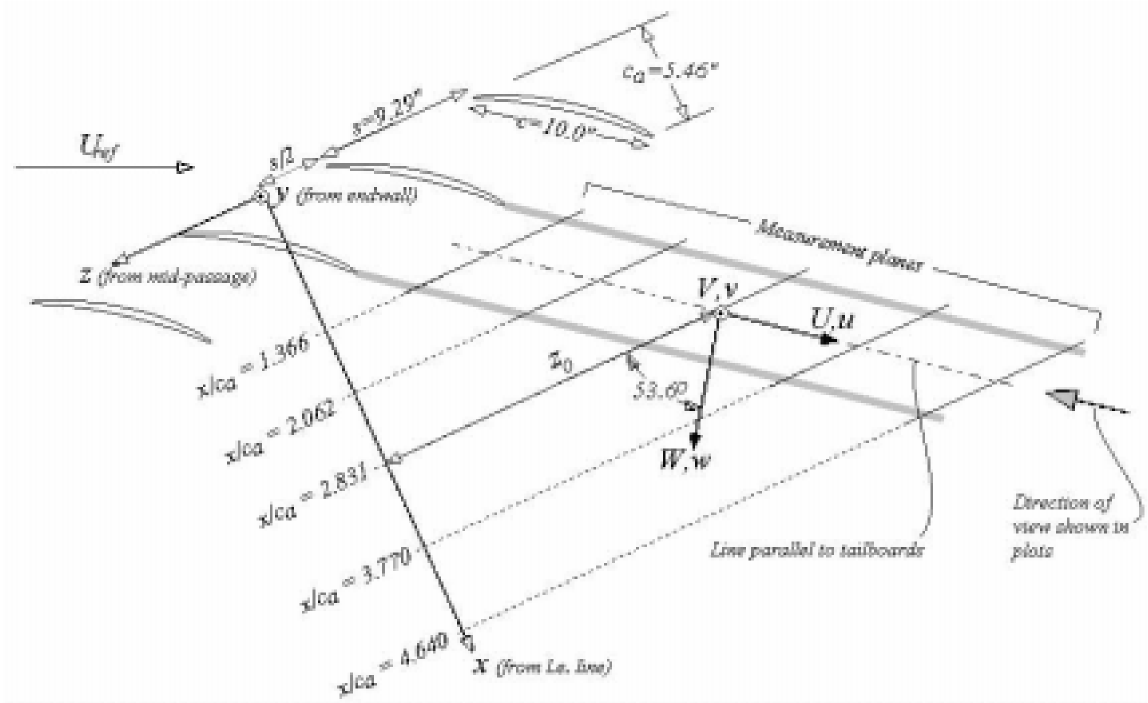


Figure 6.3

A diagram showing the single-point measurement locations.

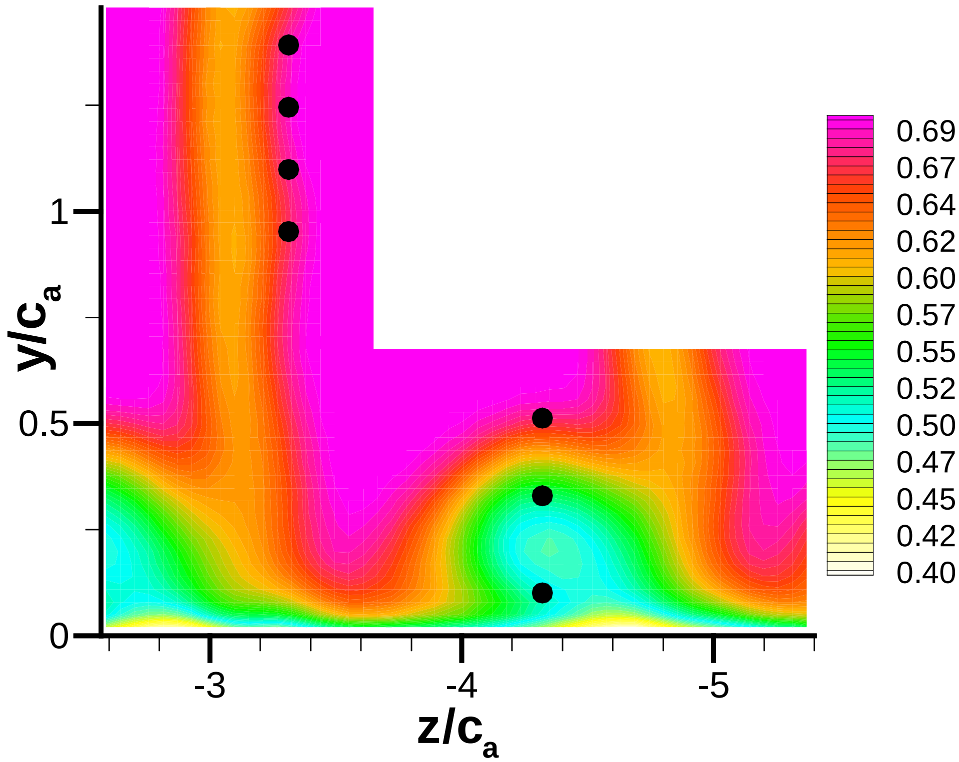


Figure 5.4

Mean streamwise velocity $U/U_\infty$ at $x/c_a = 2.831$. The black dots indicate the locations of the autospectra shown in figure 5.8.

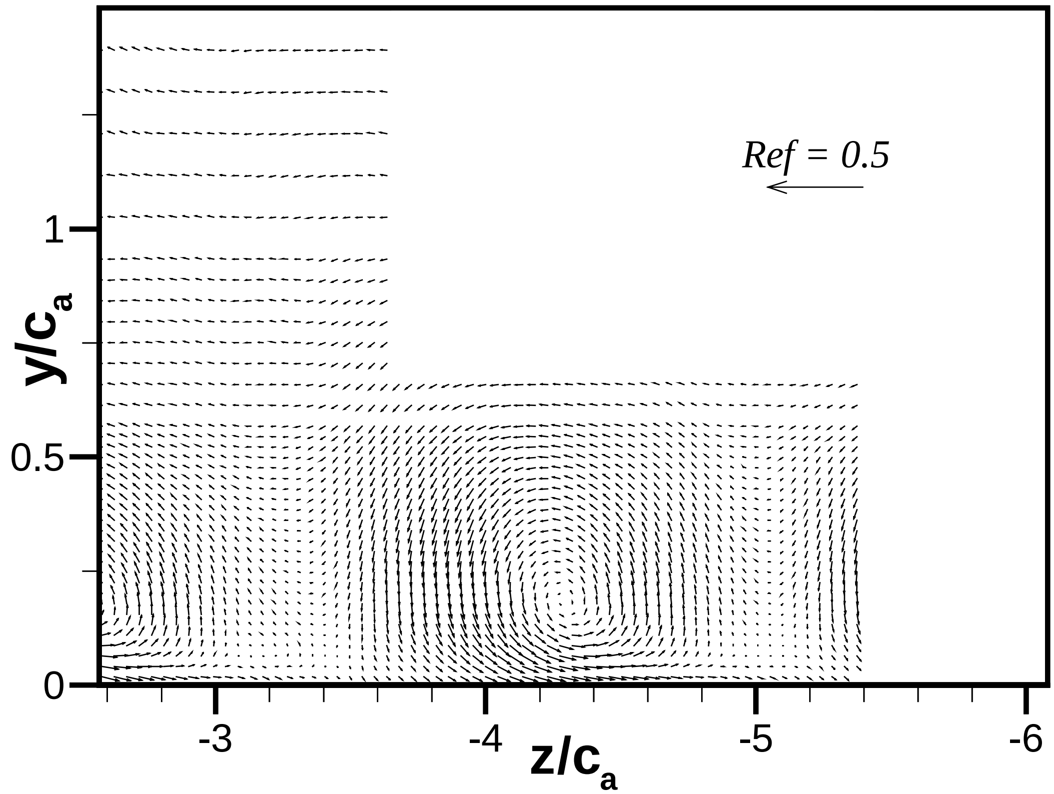


Figure 5.5

Mean cross-flow velocity vectors resolved normal to the axis of the tip leakage vortex at $x/c_a$ = 2.831. The length of the reference vector is $0.5U_\infty$. Taken from Wenger *et al*. (1998).

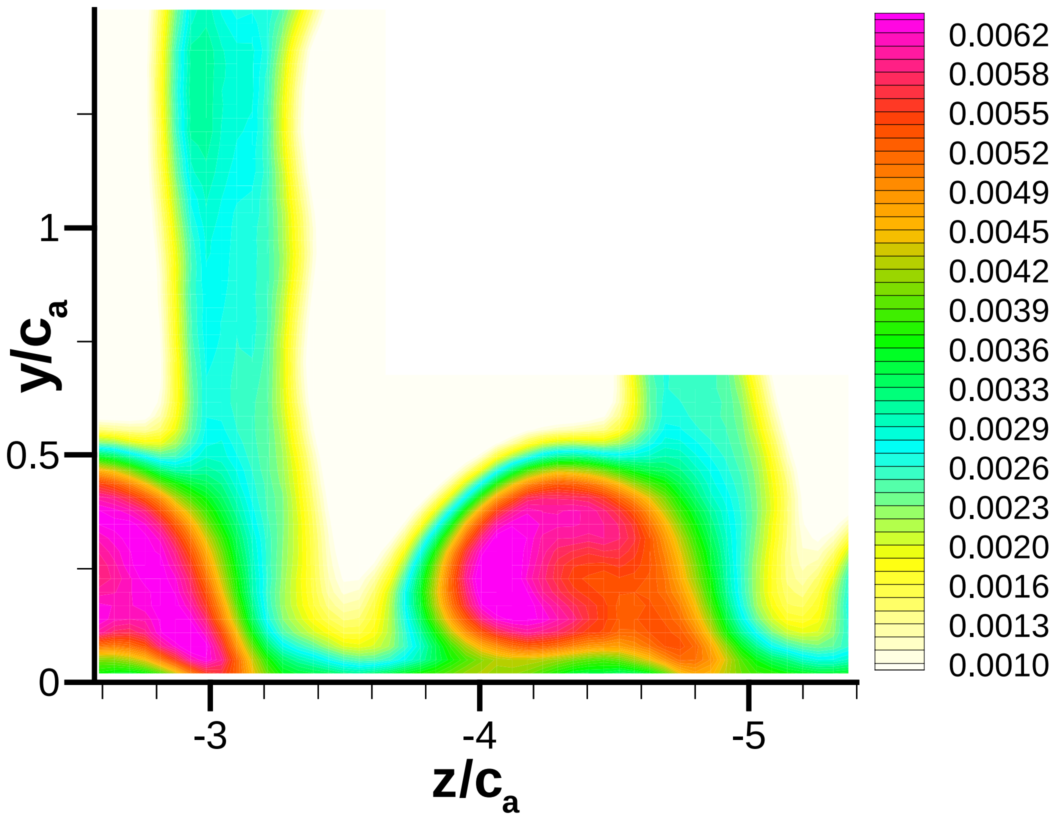


Figure 5.6

Turbulence Kinetic Energy contours normalized by $U_\infty^2$ at $x/c_a = 2.831$.

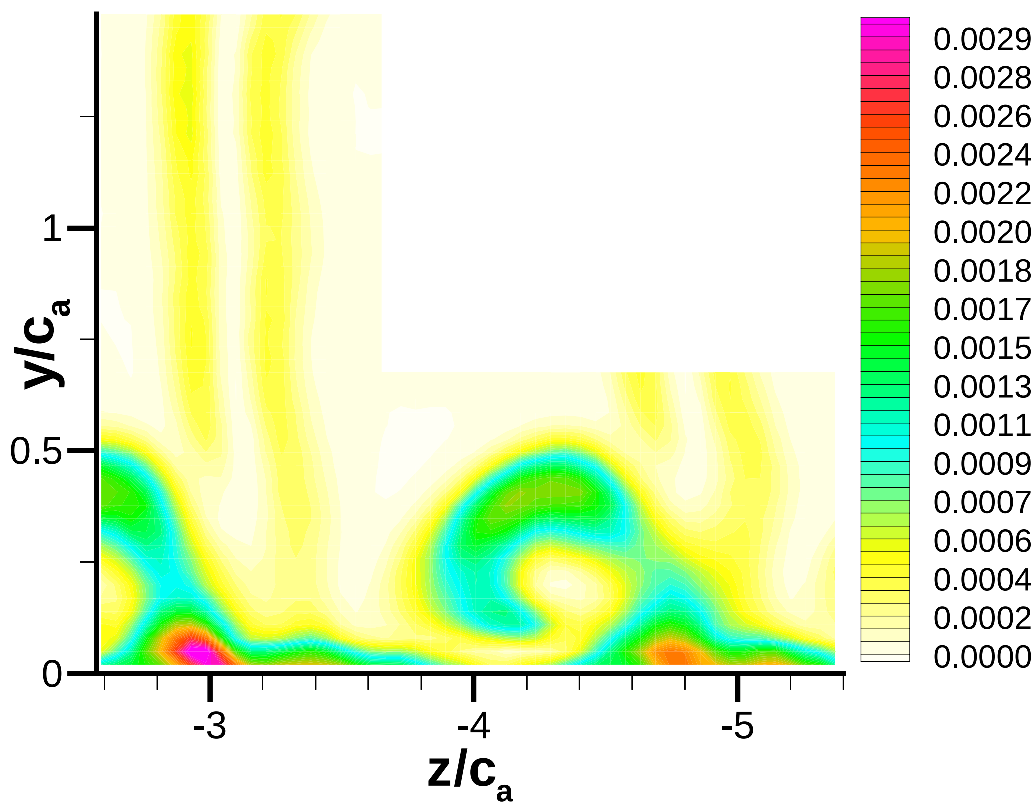


Figure 5.7

Contours of turbulence kinetic energy production.

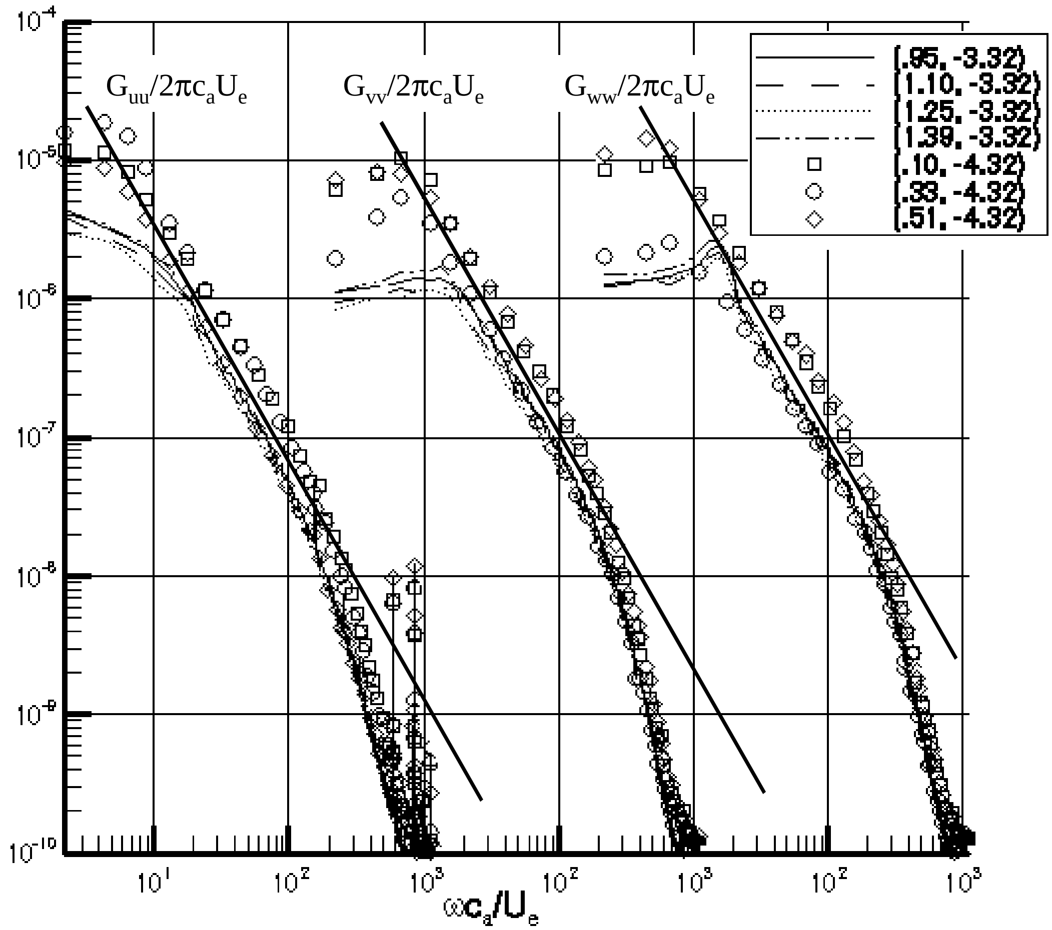


Figure 5.8

Single point autospectra. The coordinates in the legend are the locations corresponding to the black dots in figure 5.4, for which the autospectra have been calculated . The dark line drawn for each velocity component has a -5/3 slope. Taken from Wenger *et al.* (1998).

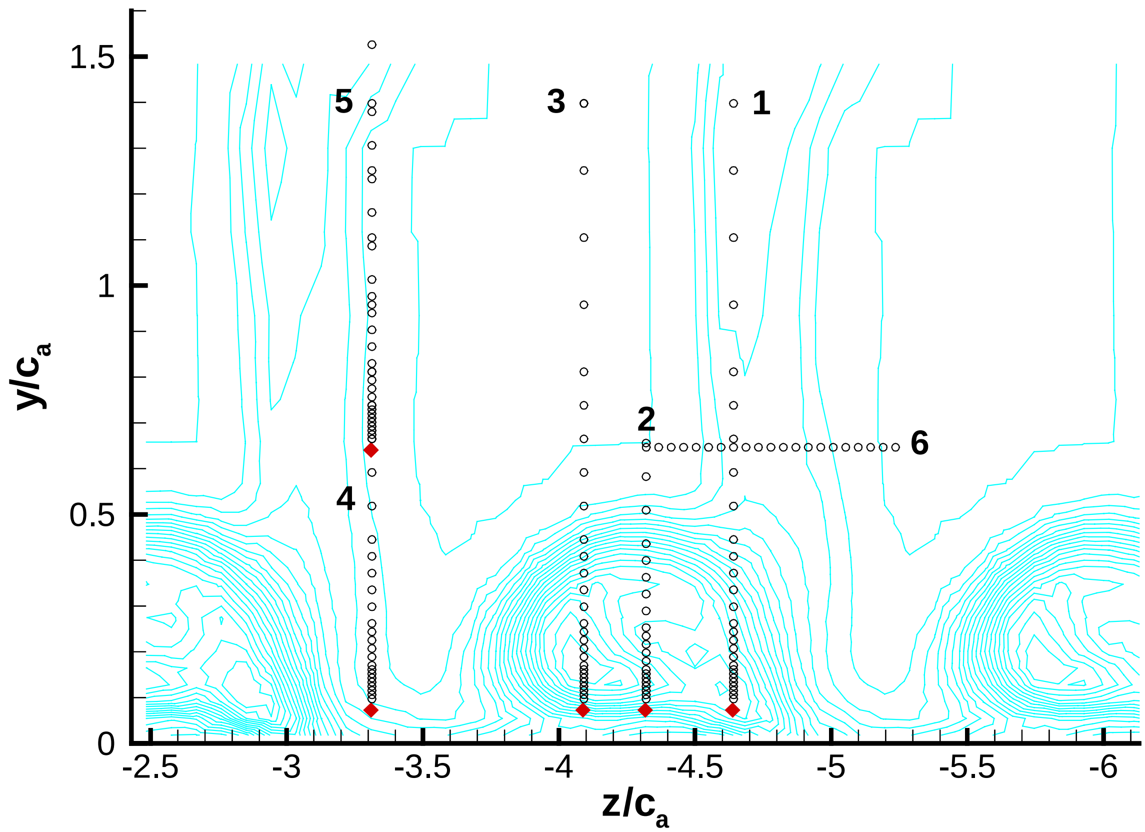


Figure 5.9

Two-point profile measurement locations. The red diamonds indicate the fixed probe locations, and the circles indicate the movable probe location. The background contours are turbulent kinetic energy.

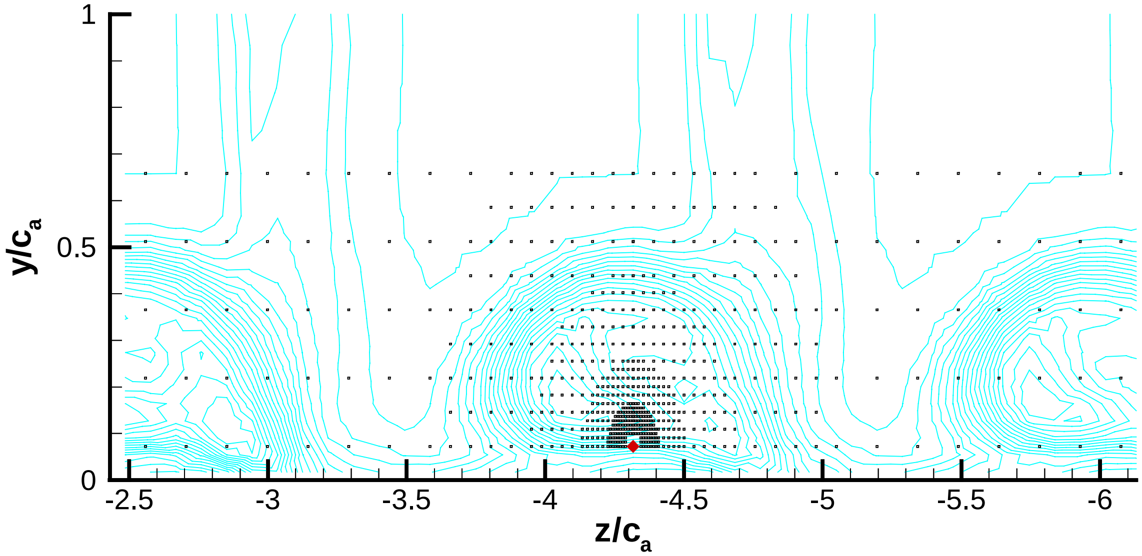


Figure 5.10

Two-point grid measurement locations. The re d diamond indicates the fixed probe location, and the black dots indicate the movable probe locations. The background contours are turbulent kinetic energy.

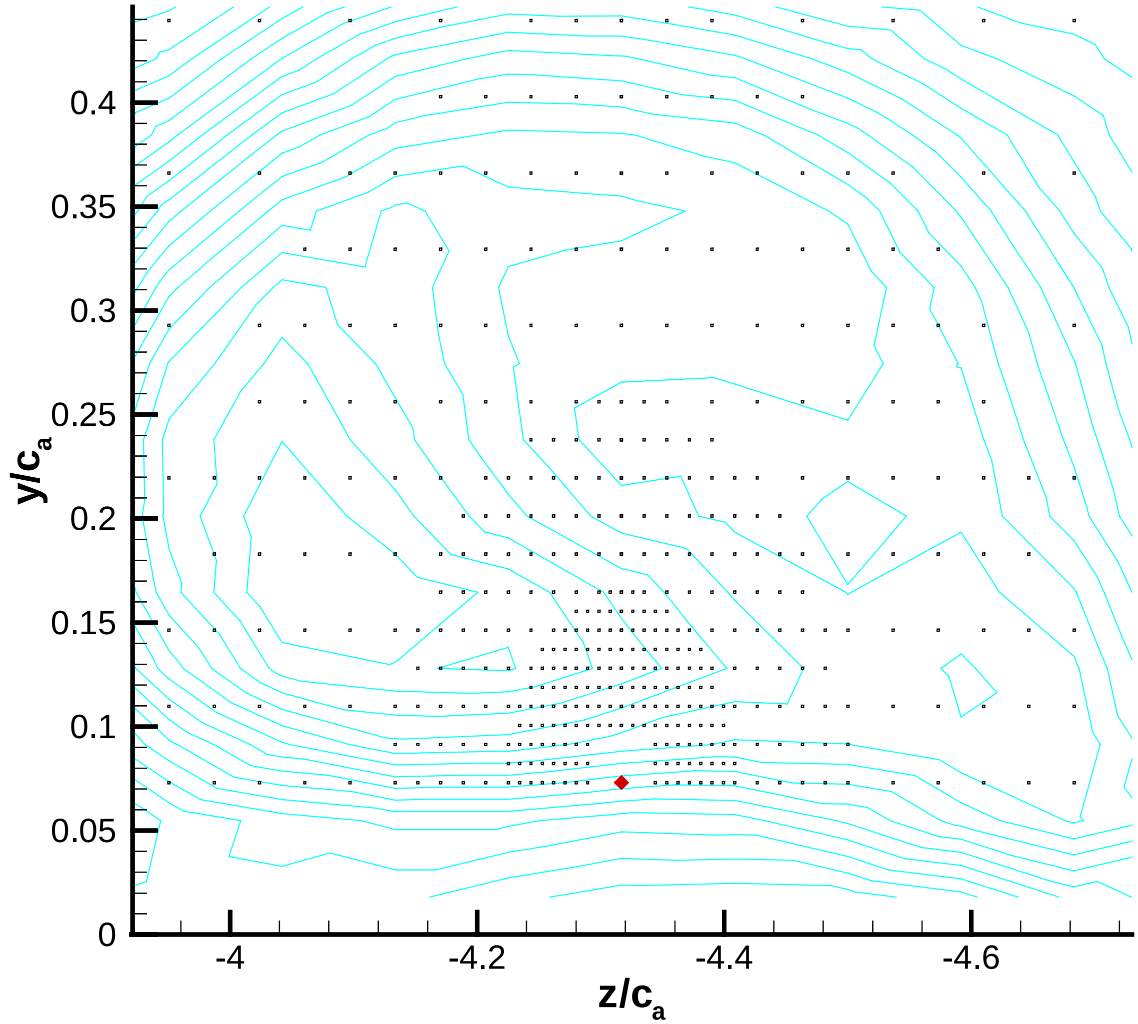


Figure 5.11

A zoomed view of the two-point grid measurement locations near the fixed probe location. The background contours are turbulent kinetic energy.

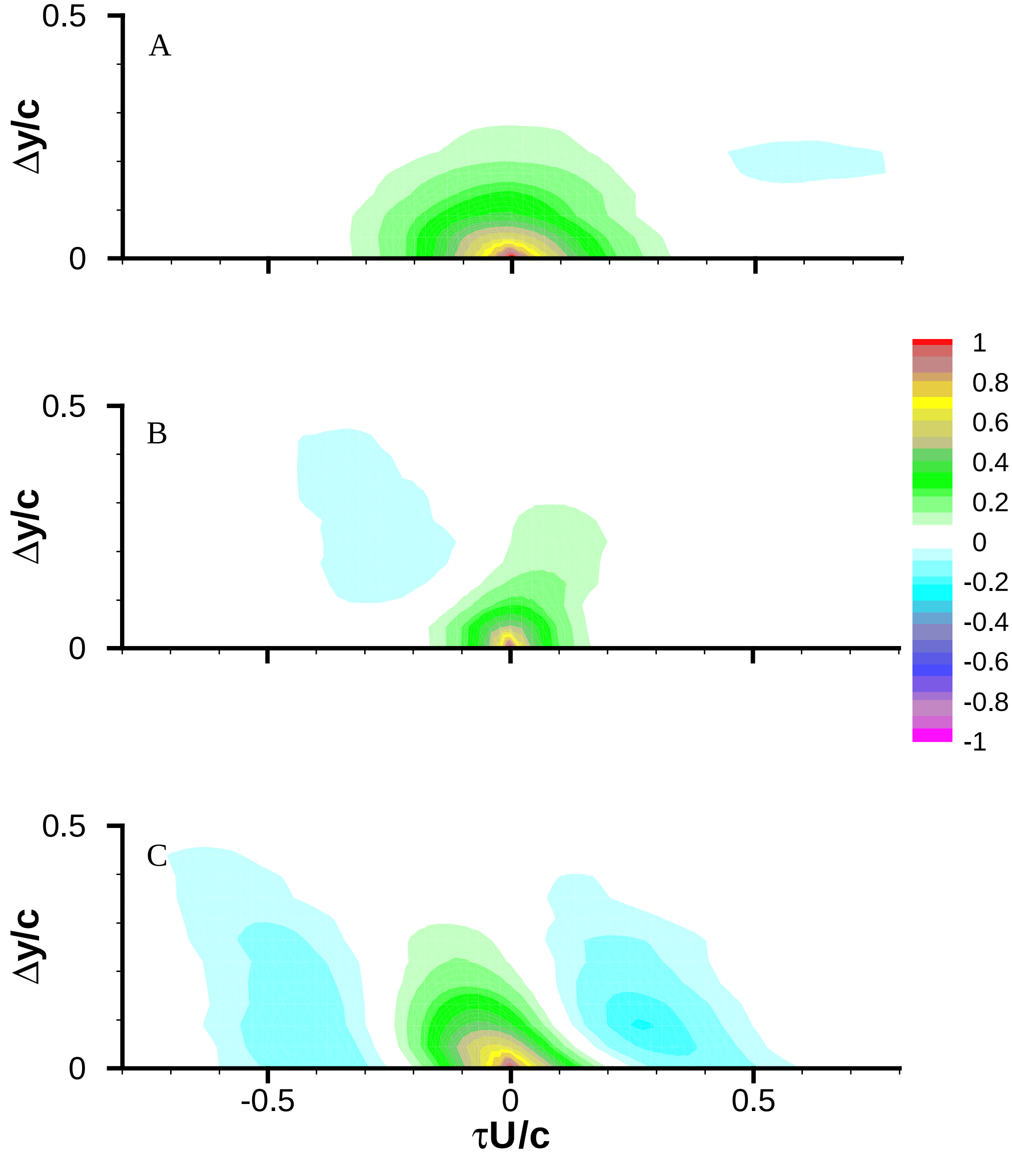


Figure 5.12

The radial space-time correlation function for profile 1, $R(0.07c_a, y', -4.65c_a, 0, \tau)$. A) the $u$ - velocity component, B) the $v$ - velocity component, and C) the $w$ - velocity component.

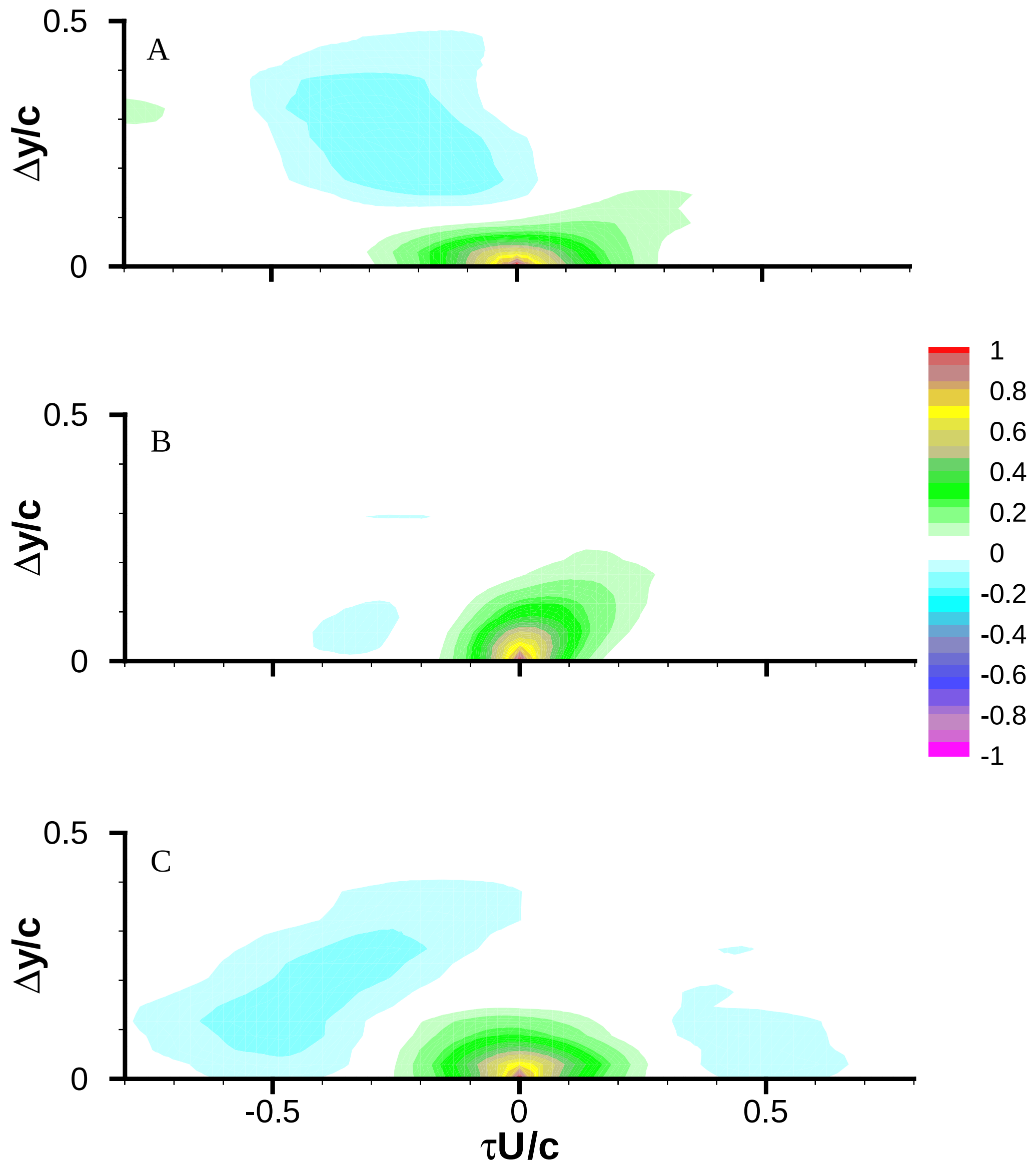


Figure 5.13

The radial space-time correlation function for profile 2, $R(0.07c_a, y', -4.32c_a, 0, \tau)$. A) the $u$ - velocity component, B) the $v$ - velocity component, and C) the $w$ - velocity component.

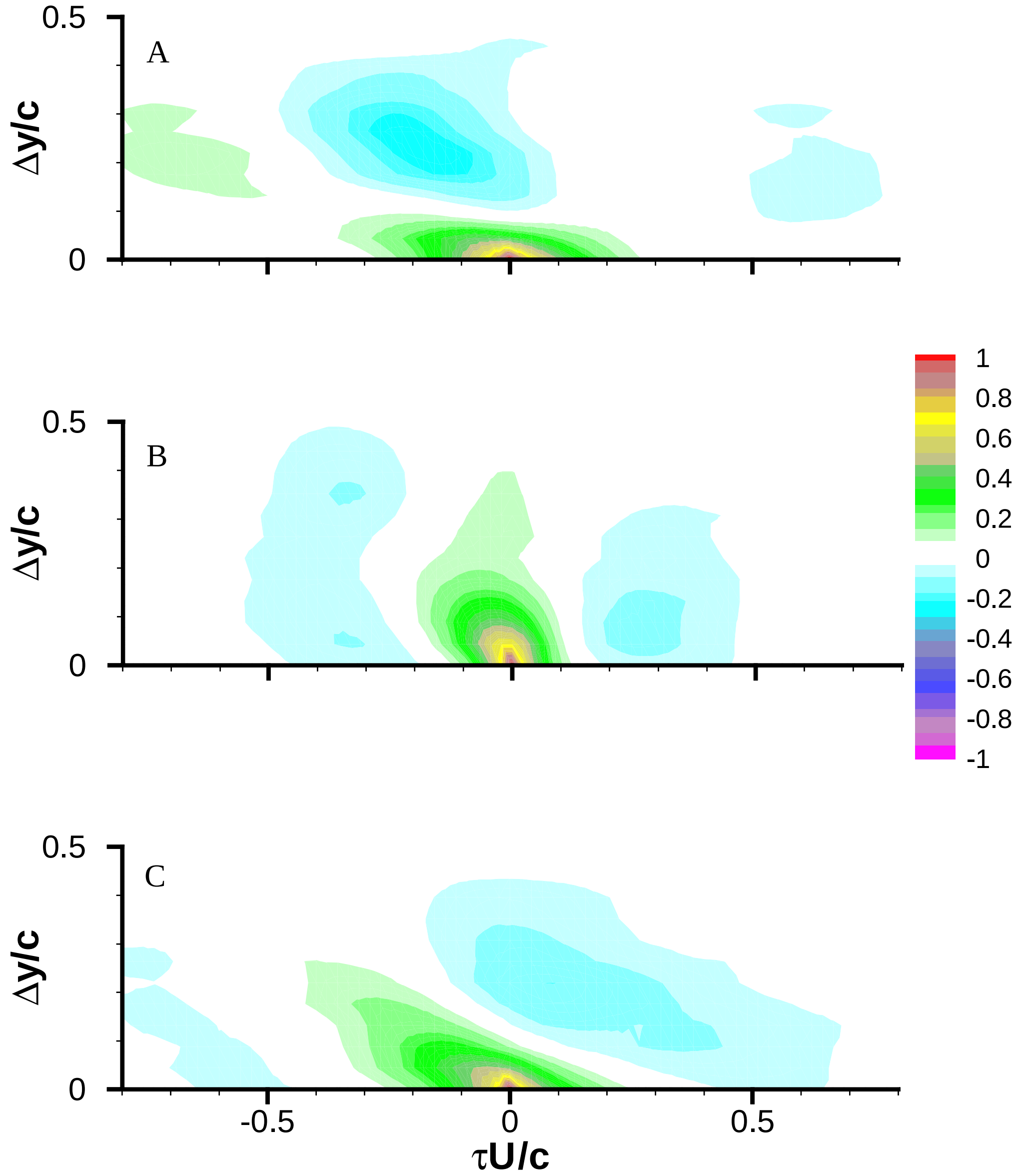


Figure 5.14

The radial space-time correlation function for profile 3, $R(0.07c_a, y', -4.10c_a, 0, \tau)$. A) the $u$ - velocity component, B) the $v$ - velocity component, and C) the $w$ - velocity component.

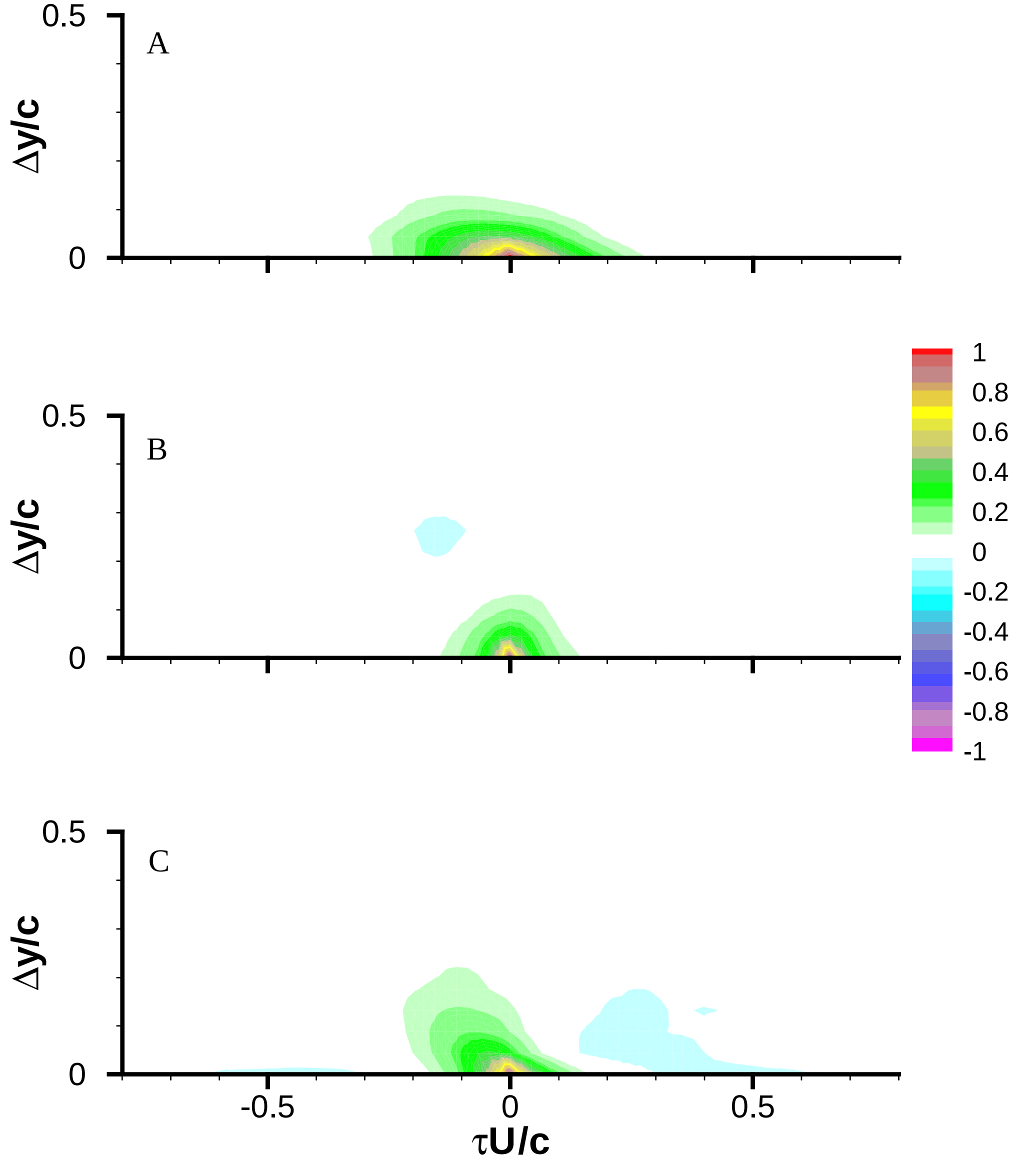


Figure 5.15

The radial space-time correlation function for profile 4, $R(0.07c_a, y', -3.30c_a, 0, \tau)$. A) the $u$ - velocity component, B) the $v$ - velocity component, and C) the $w$ - velocity component.

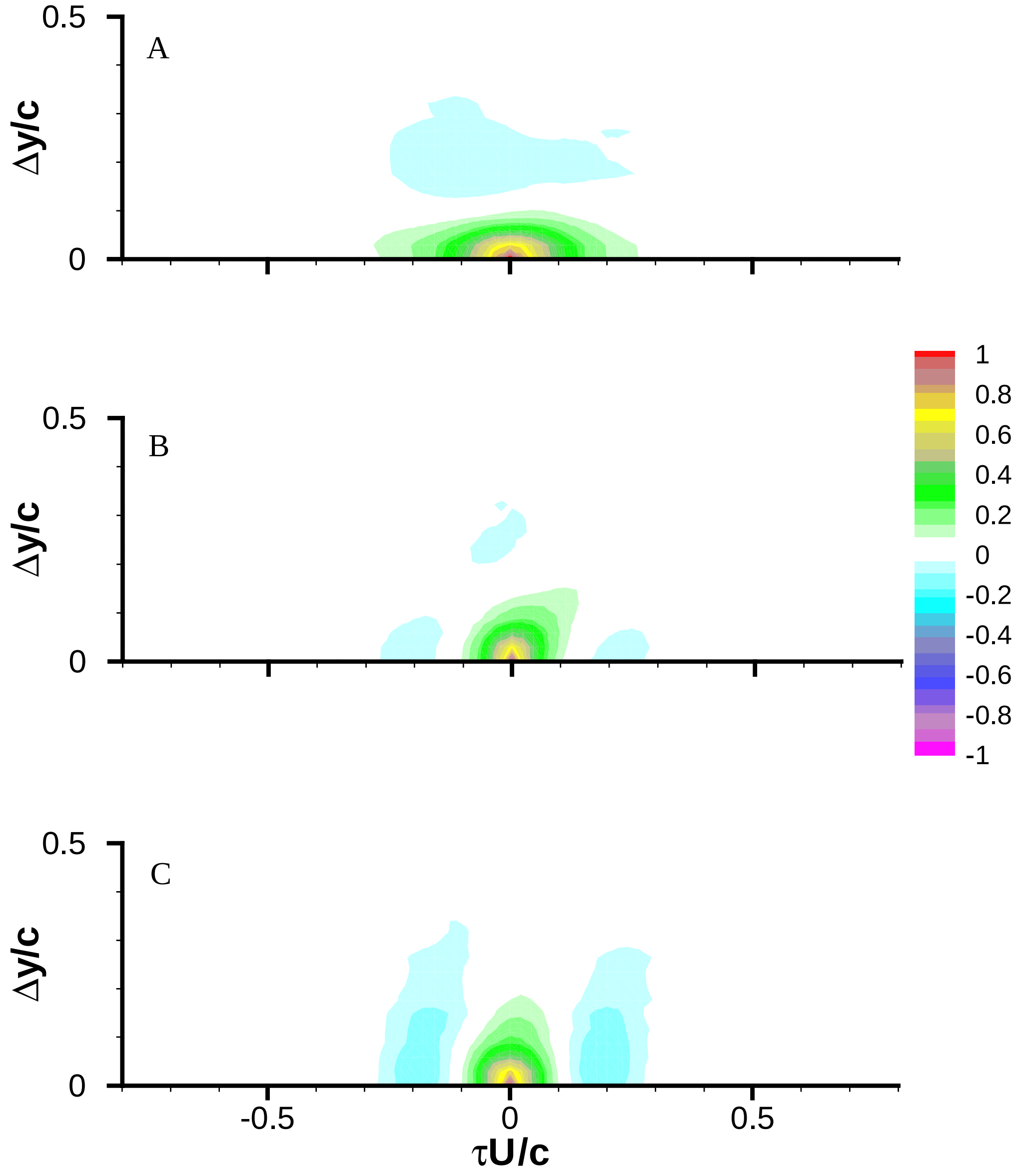


Figure 5.16

The radial space-time correlation function for profile 5, $R(0.65c_a, y', -3.30c_a, 0, \tau)$. A) the $u$ - velocity component, B) the $v$ - velocity component, and C) the $w$ - velocity component.

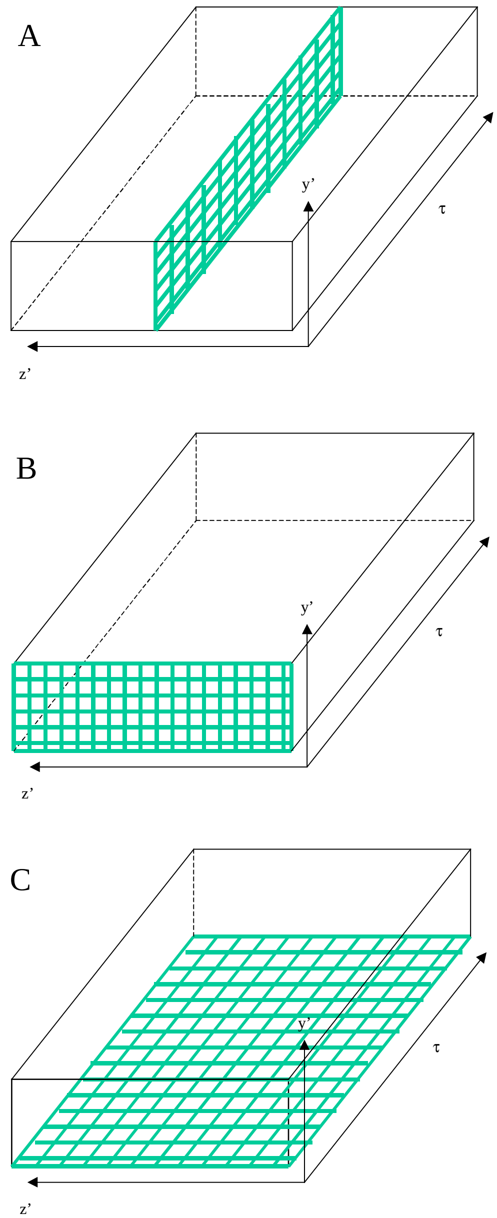


Figure 5.17

Diagrams showing the displayed two-dimensional slices of the three-dimensional space-time correlation space. A) The radial plane represented by $R(0.07c_a, y', -4.32c_a, 0, \tau)$. B) The front plane represented by $R(0.07c_a, y', -4.32c_a, z', 0)$. C) The bottom plane represented by $R(0.07c_a, 0, -4.32c_a, z', \tau)$.

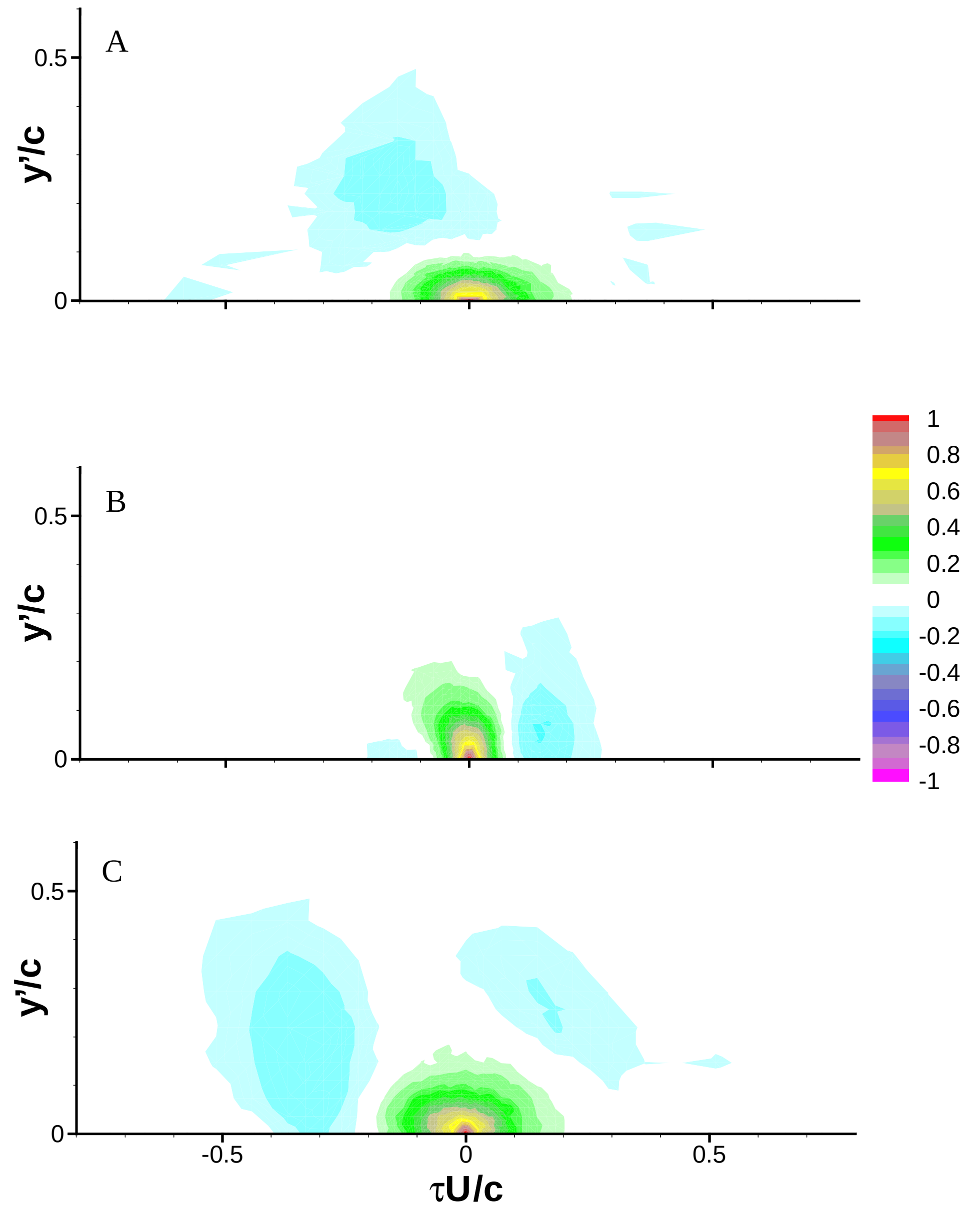


Figure 5.18

The front plane (figure 5.17B) of the three-dimensional space-time correlation space, $R(0.07c_a, y', -4.32c_a, z', 0)$. A) the $u$ - velocity component, B) the $v$ - velocity component, and C) the $w$ - velocity component.

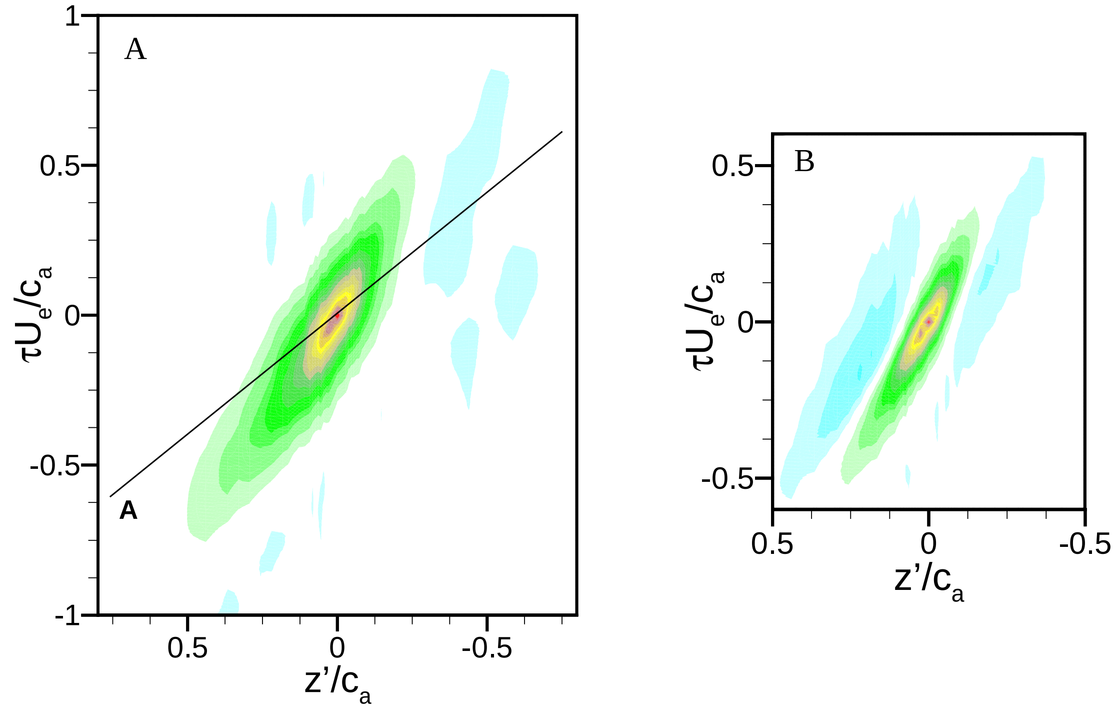


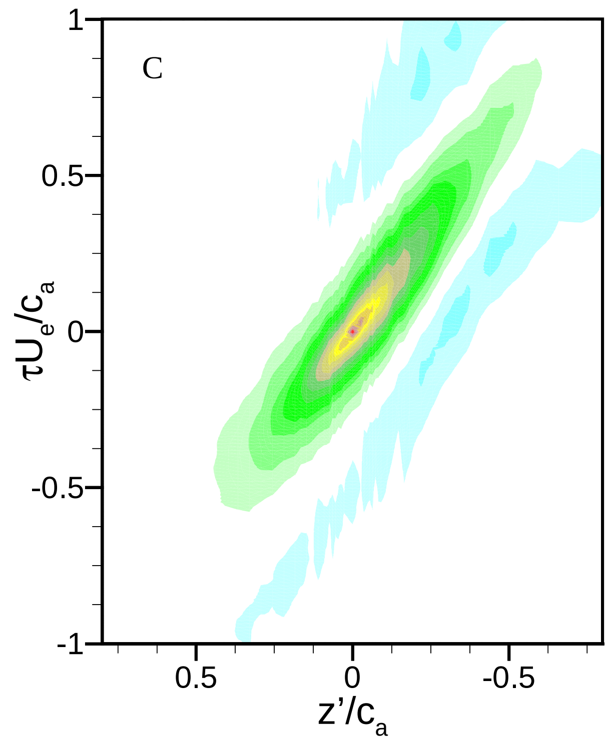


Figure 5.19
The bottom plane (figure 5.17C) of the three-dimensional space-time correlation space, $R(0.07c_a, 0, -4.32c_a, z', \tau)$. A) the $u$ - velocity component, Line A indicates the cut through the correlation space taken for the stator frame of reference, B) the $v$ - velocity component, and C) the $w$ - velocity component.

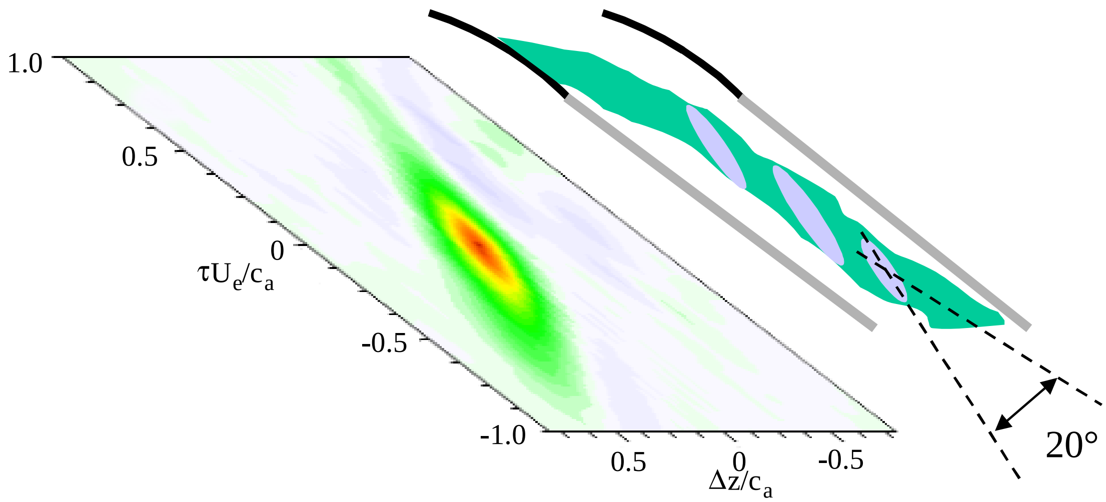


Figure 5.20

*u* component data from figure 5.19A replotted to show time delay in the mean-flow direction as per Taylor's hypothesis and sketch showing implied eddy orientation relative to vortex axis. Taken from Wenger *et al*. (1998).

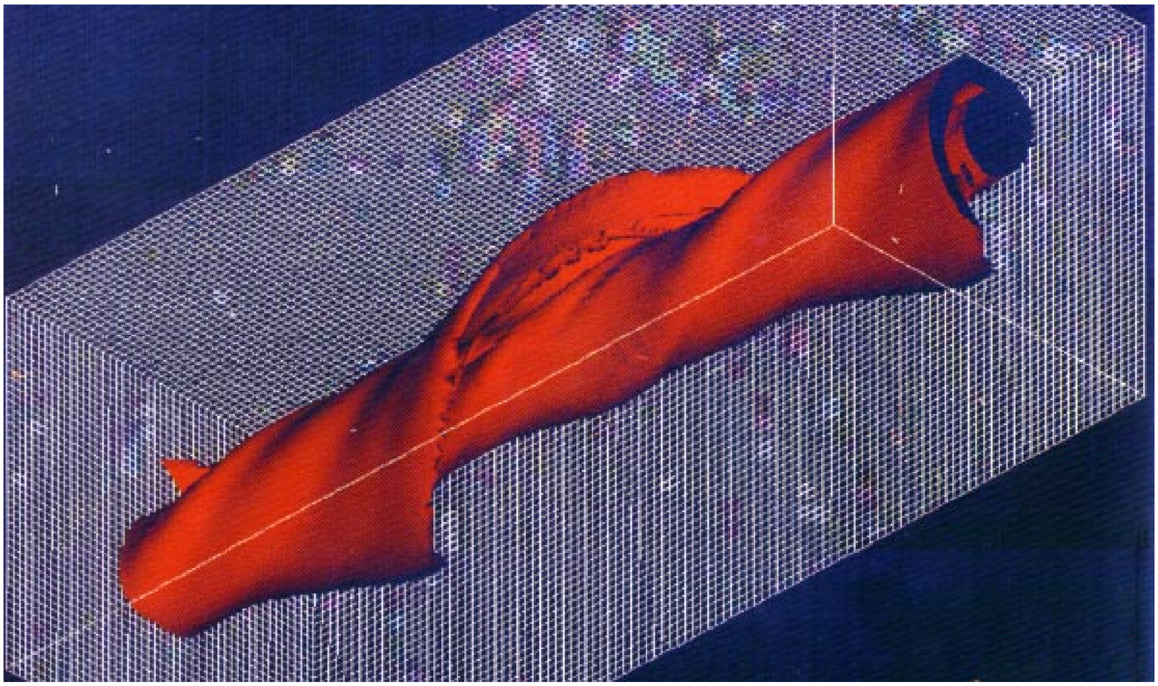

Figure 5.21

A picture of a direct numerical simulation of a vortex with high axial velocity gradients performed by Ragab (1995).

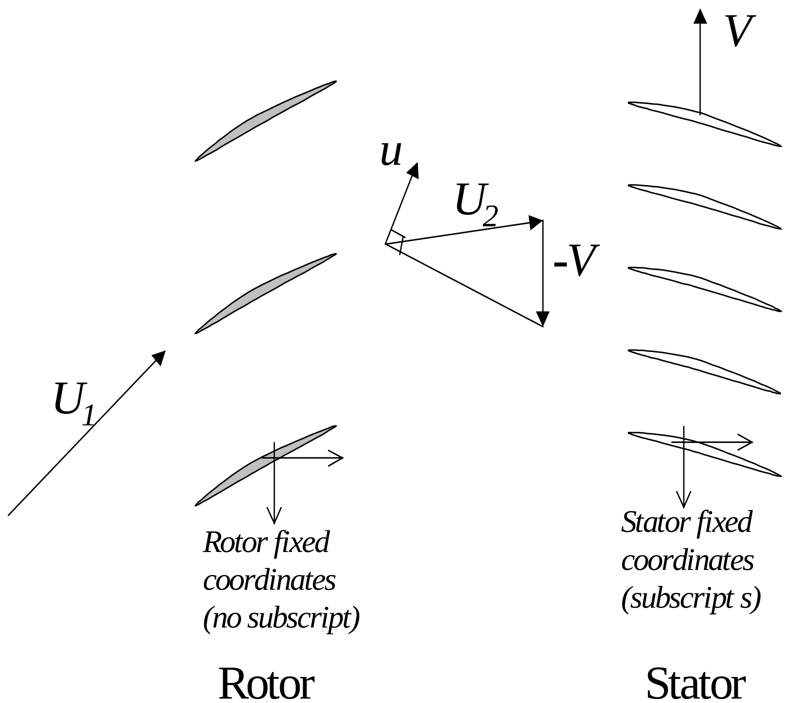


Figure 5.22

Schematic showing the simulated motion of the rotor and stator blades. Taken from Wenger *et al*. (1998).

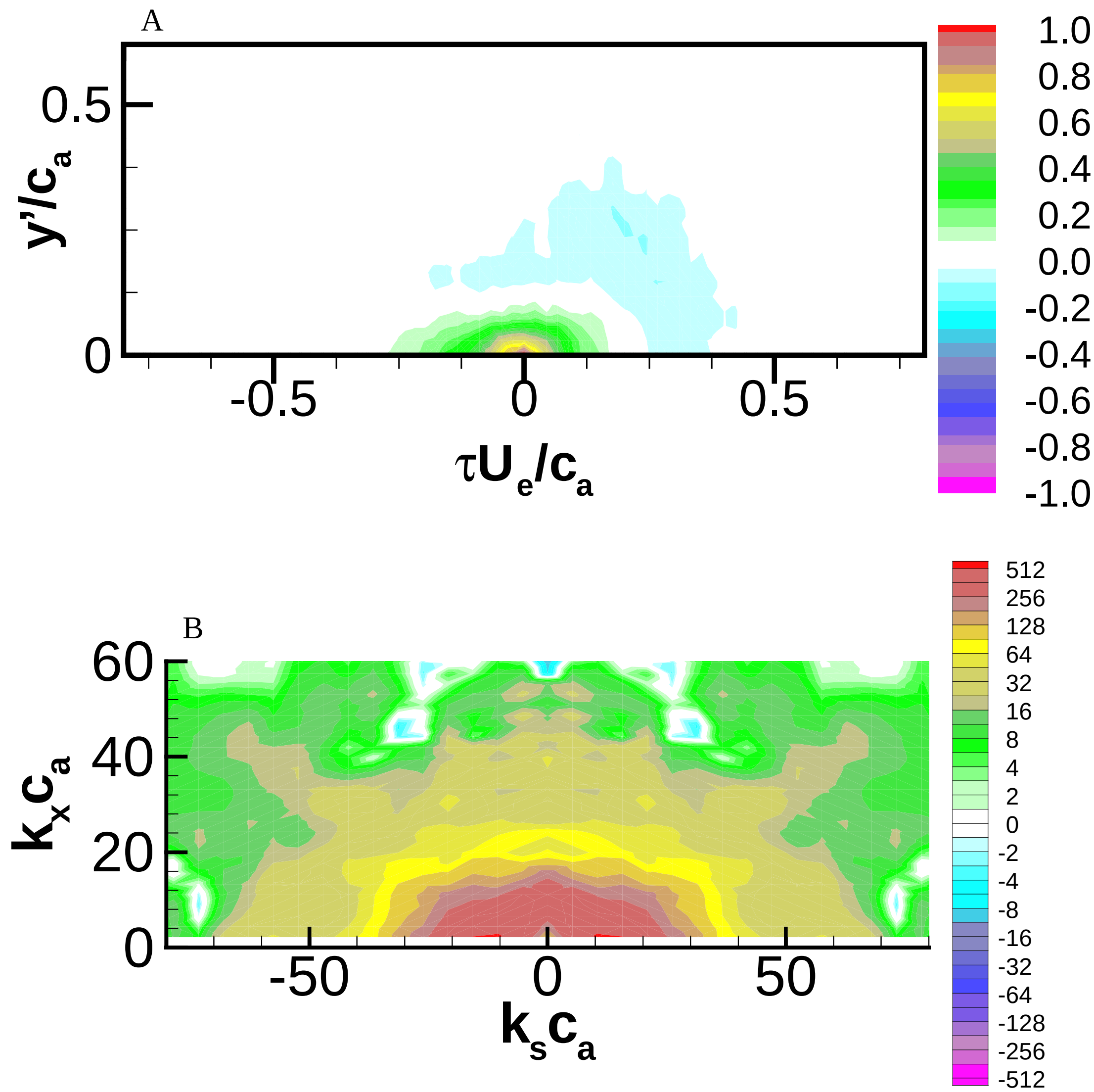


Figure 5.23

A) Radial space-time correlation of the stator upwash velocity fluctuations in the stator frame of reference. B) The corresponding wave number frequency spectrum.

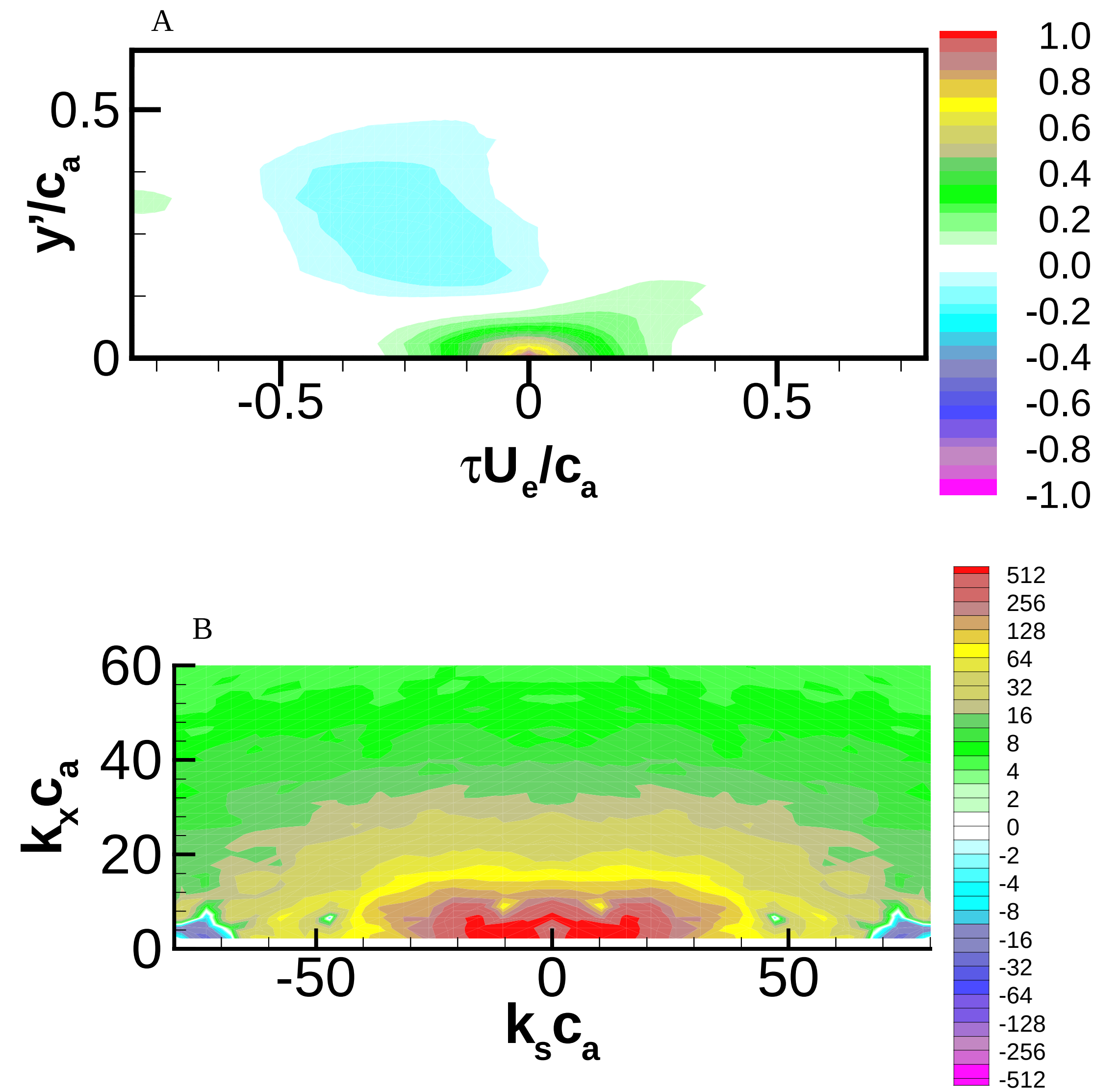


Figure 5.24

A) Radial space-time correlation of the stator upwash velocity fluctuations in the rotor frame of reference. B) The corresponding wave number frequency spectrum.

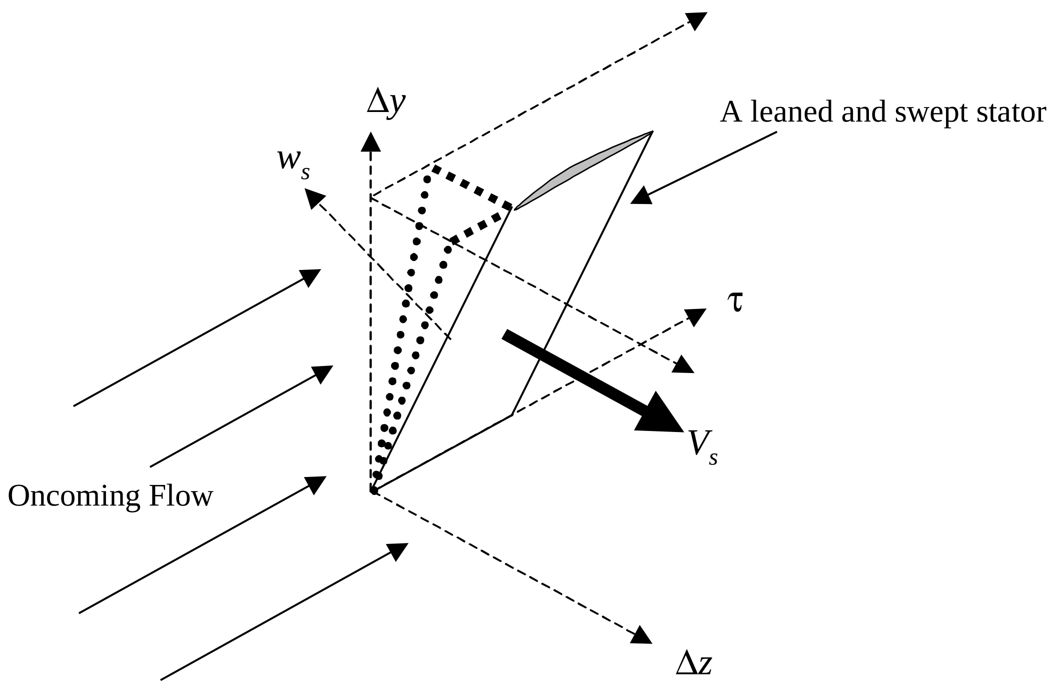


Figure 5.25

A diagram showing how the stator upwash velocity component, $w_s$, is determined by simulated tangential stator velocity, $V_s$, and by the lean and sweep of the stator. Coincidentally, for an unleaned and unswept stator, the stator upwash velocity component turns out to be the $u$ - velocity component.

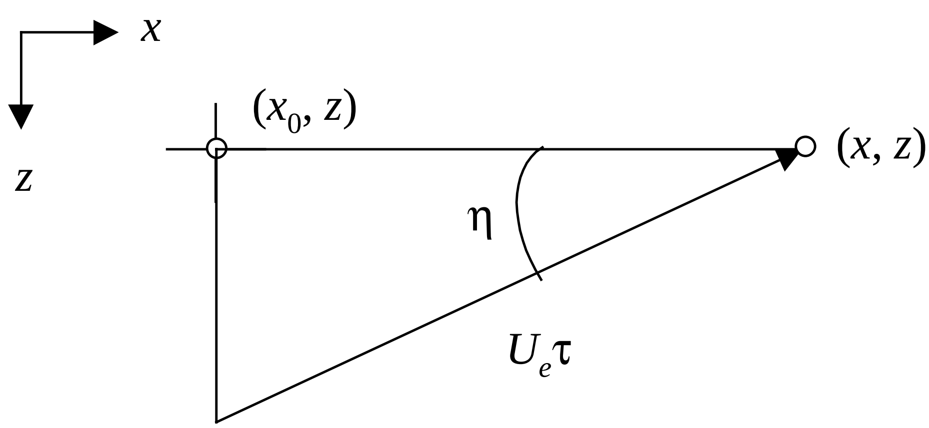


Figure 5.26

Diagram depicting the implications of Taylor's hypothesis for determining flow velocity at locations other than the measurement location, $x_0$. The angle between the mean velocity direction, *u*, and the *x* direction is denoted by $\eta$.

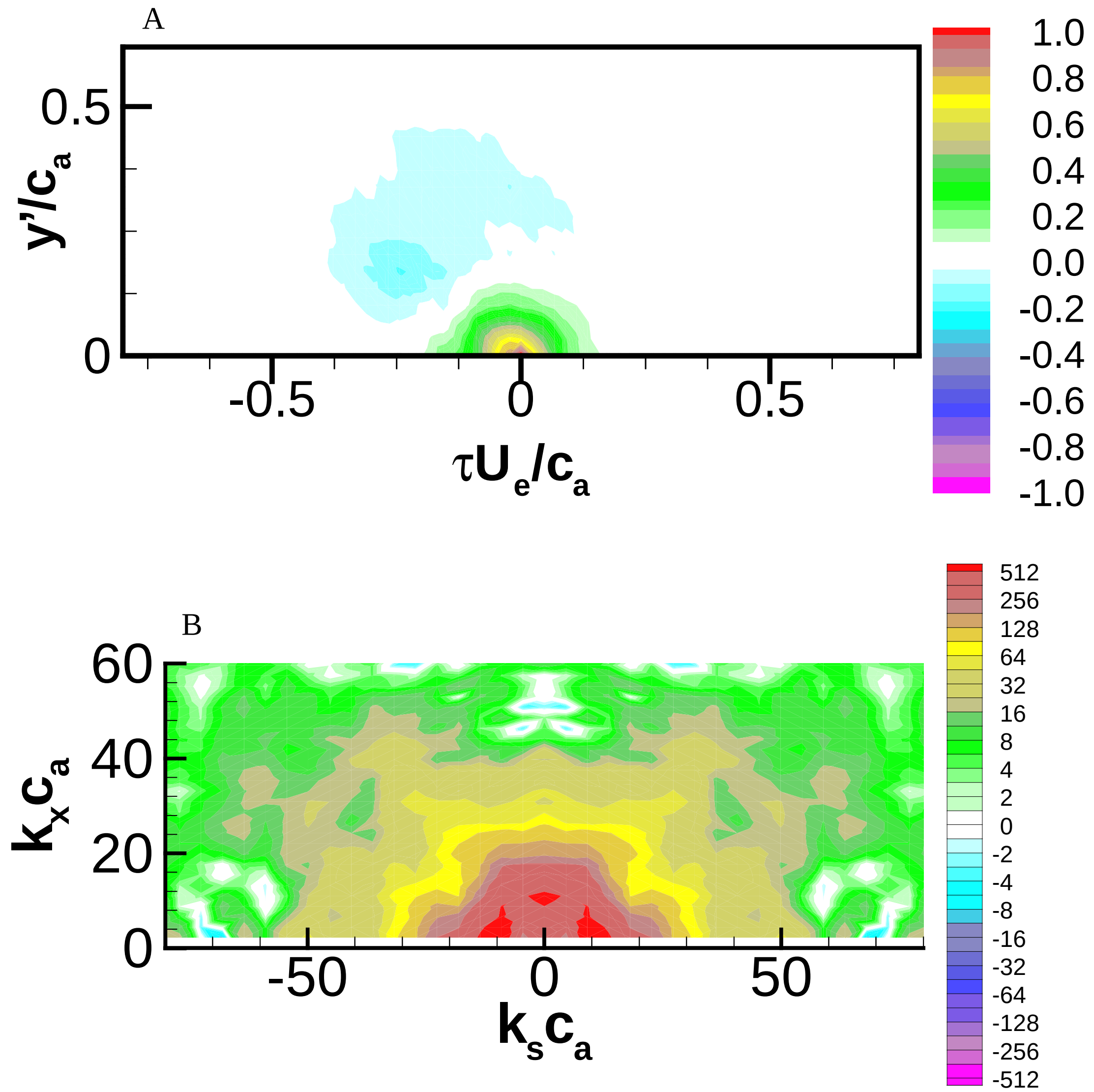


Figure 5.27

A) Space-time correlation of the stator upwash velocity fluctuations in the stator frame of reference for a stator with 30° lean. B) The corresponding wave number frequency spectrum.

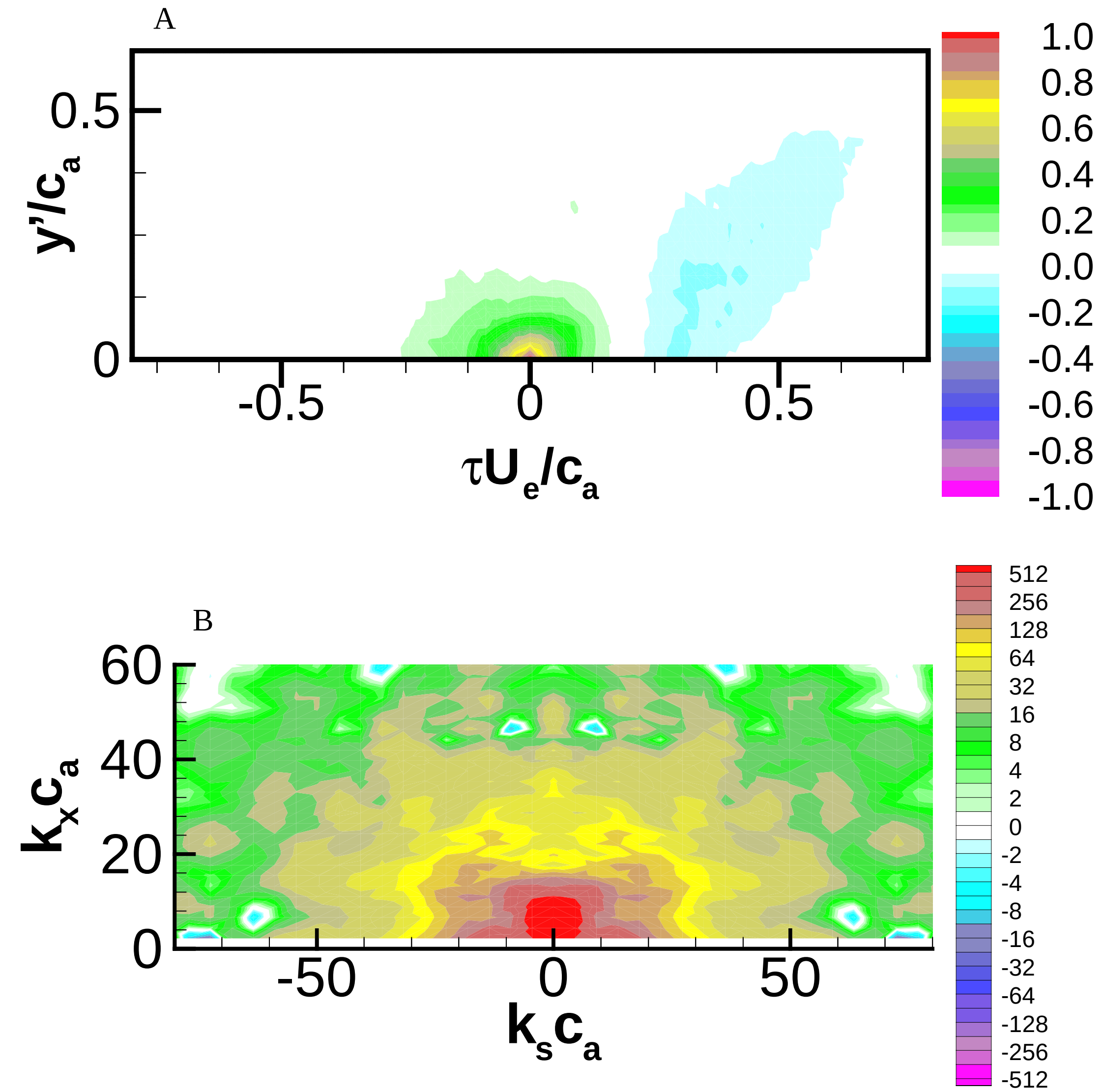


Figure 5.28

A) Space-time correlation of the stator upwash velocity fluctuations in the stator frame of reference for a stator with -30° lean. B) The corresponding wave number frequency spectrum.

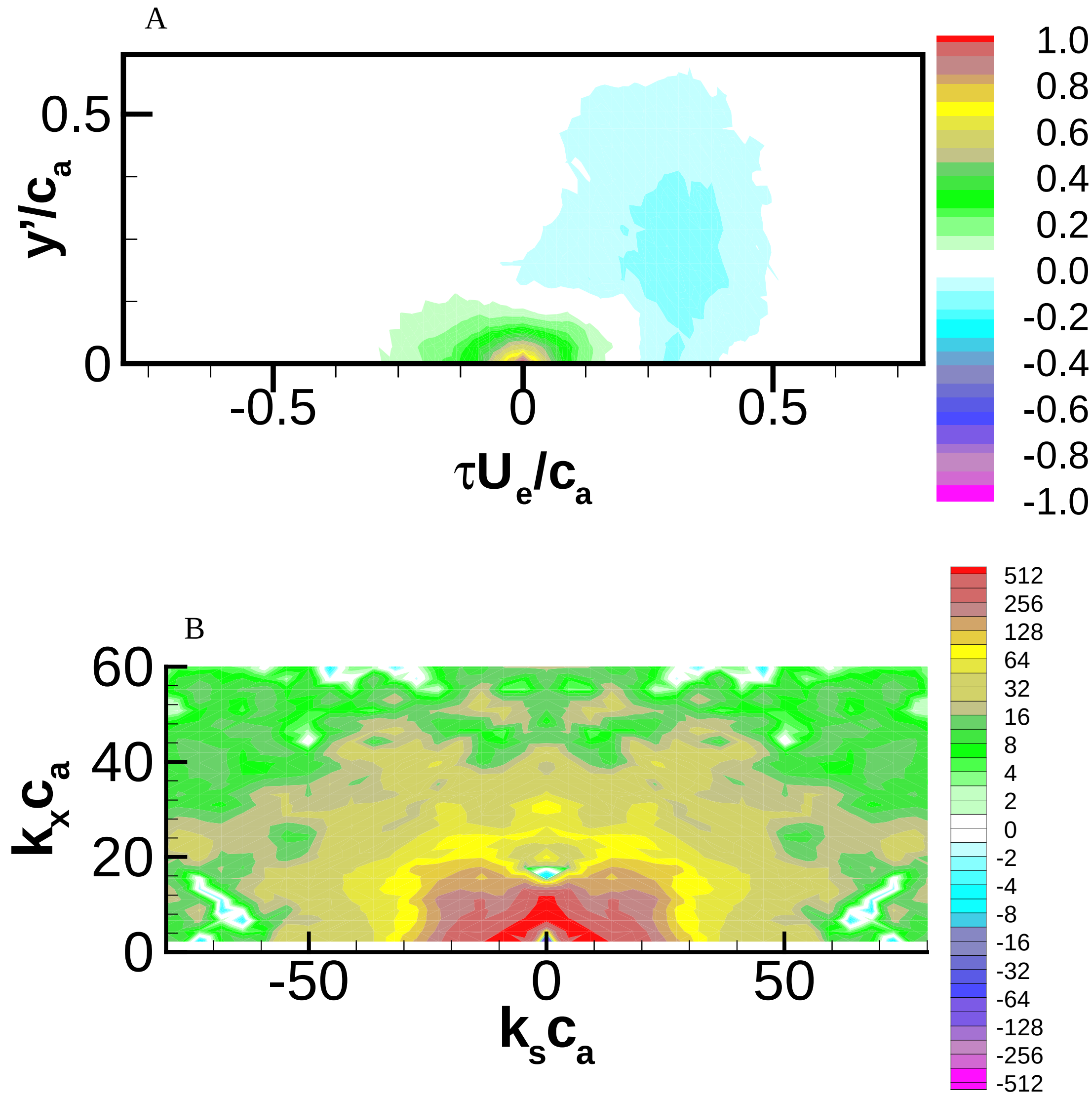


Figure 5.29

A) Space-time correlation of the stator upwash velocity fluctuations in the stator frame of reference for a stator with 30° sweep. B) The corresponding wave number frequency spectrum.

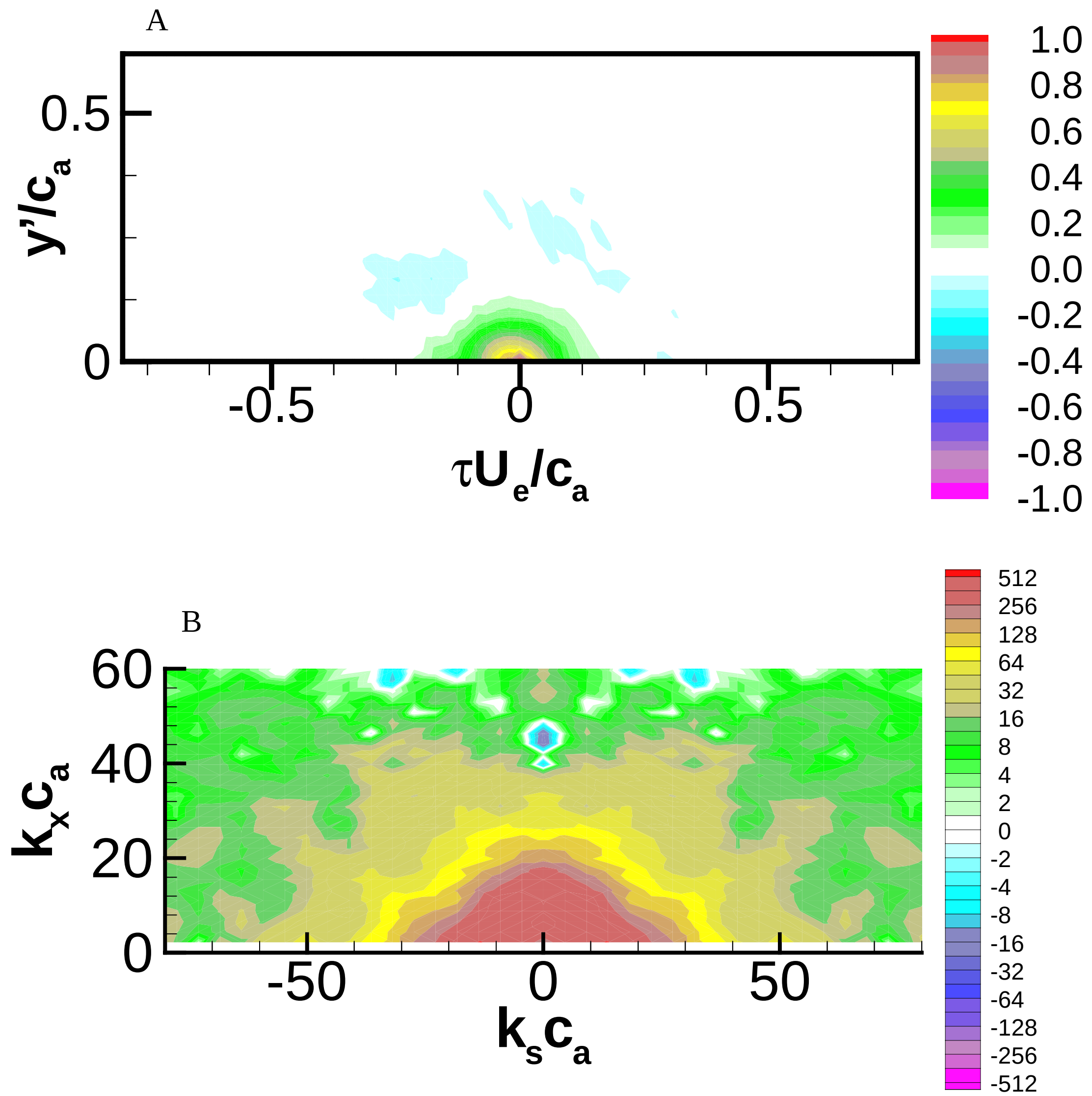


Figure 5.30

A) Space-time correlation of the stator upwash velocity fluctuations in the stator frame of reference for a stator with -30° sweep. B) The corresponding wave number frequency spectrum.

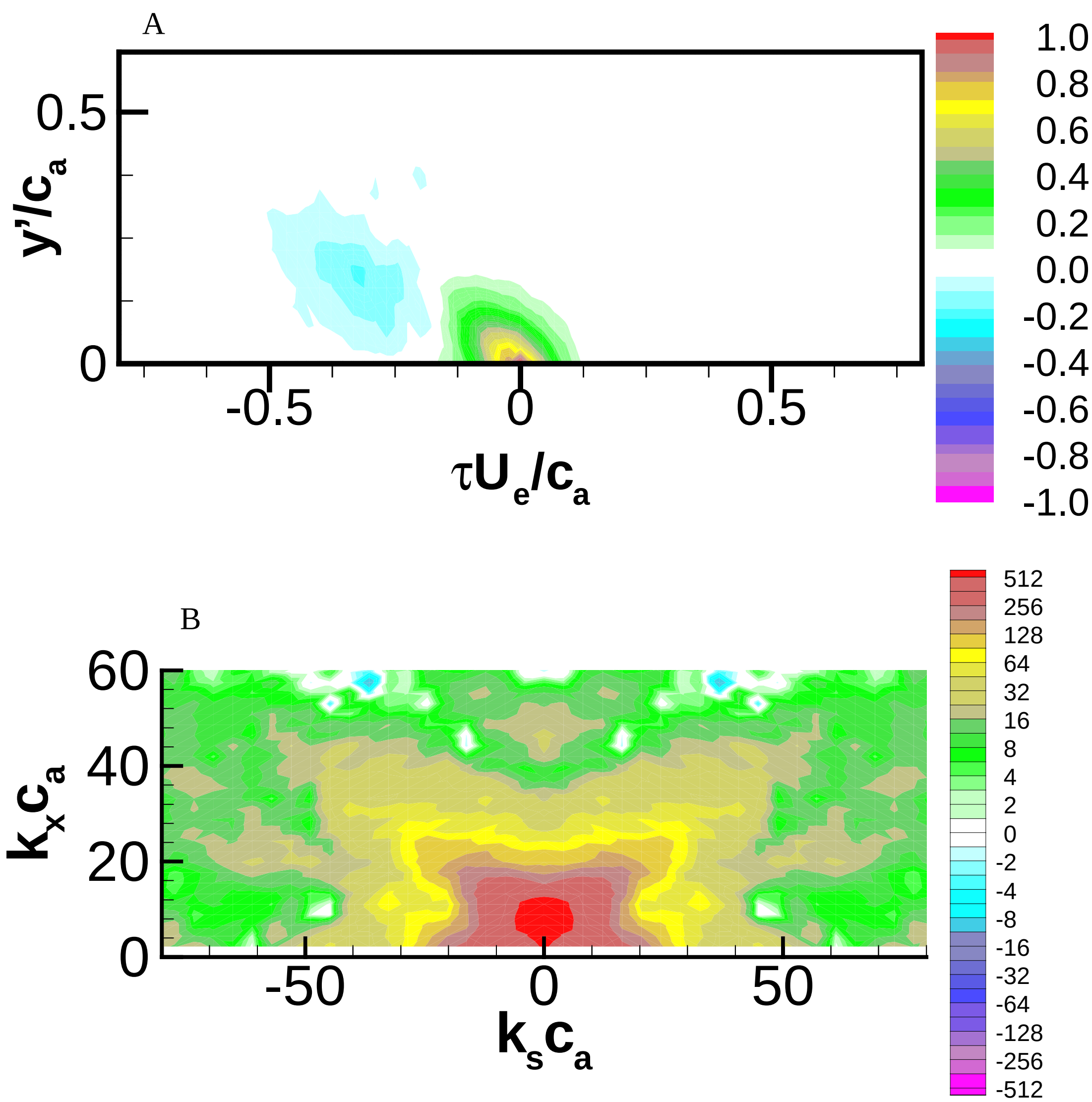


Figure 5.31

A) Space-time correlation of the stator upwash velocity fluctuations in the stator frame of reference for a stator with 30° lean and -30° sweep. B) The corresponding wave number frequency spectrum.

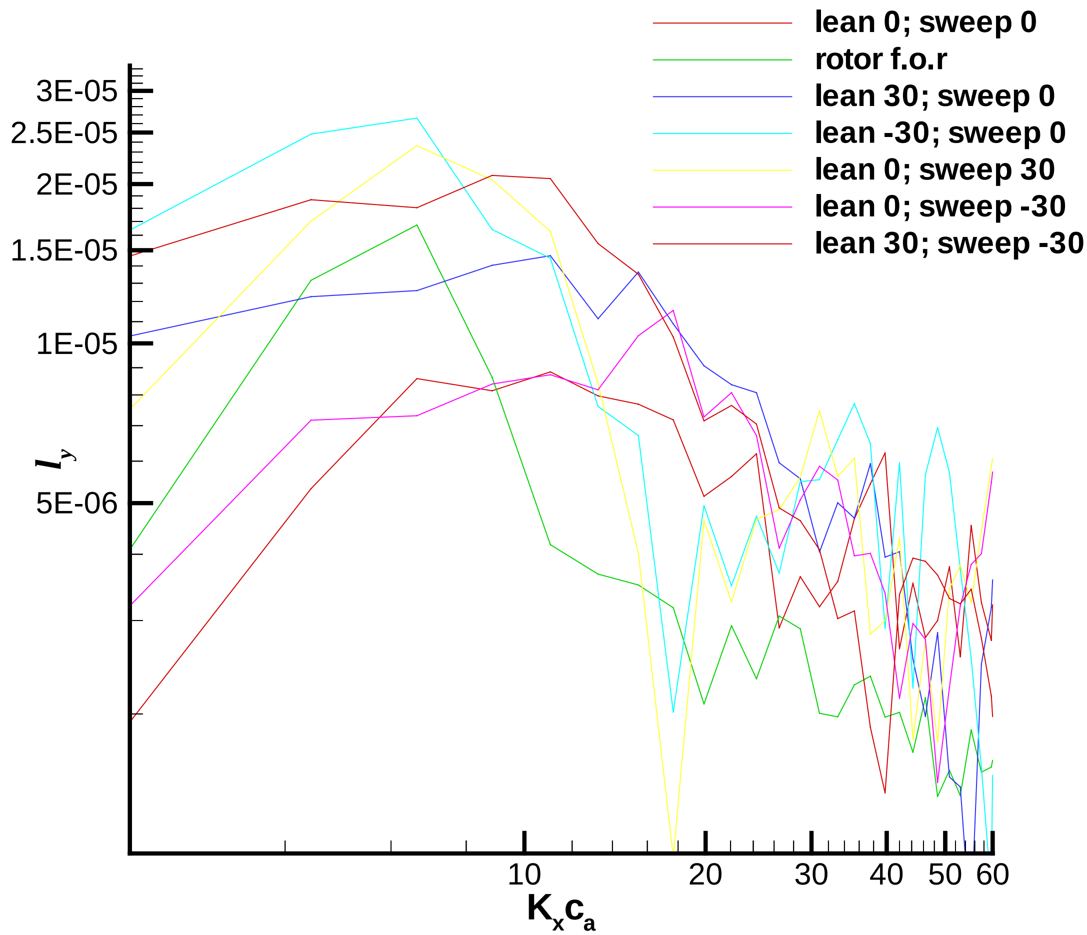


Figure 5.32

Correlation length scales corresponding to the various stator upwash wave number frequency spectra.